



1 Using reference radiosondes to characterise NWP model uncertainty for improved satellite
2 calibration and validation.

3

4 Fabien Carminati¹, Stefano Migliorini¹, Bruce Ingleby², William Bell², Heather Lawrence², Stuart
5 Newman¹, James Hocking¹, and Andrew Smith¹

6

7 ¹Met Office, Exeter, EX1 3PB, UK

8 ²ECMWF, Reading, RG2 9AX, UK

9

10 Abstract

11 The characterisation of errors and uncertainties in numerical weather prediction (NWP) model fields
12 is a major challenge that is addressed as part of the Horizon 2020 Gap Analysis for Integrated
13 Atmospheric ECV CLimate Monitoring (GAIA-CLIM) project. In that regard, observations from the
14 GCOS (Global Climate Observing System) Reference Upper-Air Network (GRUAN) radiosondes are
15 being used at the Met Office and European Centre for Medium-range Weather Forecasts (ECMWF)
16 to assess errors and uncertainties associated with model data.

17 The software introduced in this study and referred to as the GRUAN Processor has been developed
18 to collocate GRUAN radiosonde profiles and NWP model fields, simulate top-of-atmosphere
19 brightness temperature at frequencies used by space-borne instruments, and propagate GRUAN
20 uncertainties in that simulation. A mathematical framework used to estimate and assess the
21 uncertainty budget of the comparison of simulated brightness temperature is also proposed.

22 One year of GRUAN radiosondes and matching NWP fields from the Met Office and ECMWF have
23 been processed and analysed for the purposes of demonstration of capability. We present
24 preliminary results confirming the presence of known biases in the temperature and humidity
25 profiles of both NWP centres. The night-time difference between GRUAN and Met Office (ECMWF)
26 simulated brightness temperature at microwave frequencies predominantly sensitive to
27 temperature is on average smaller than 0.1K (0.4K). Similarly, this difference is on average smaller
28 than 0.5K (0.4K) at microwave frequencies predominantly sensitive to humidity.

29 The uncertainty estimated for the Met Office – GRUAN difference ranges from 0.08 to 0.13K for
30 temperature sensitive frequencies and from 1.6 to 2.5K for humidity sensitive frequencies. From the
31 analysed sampling, 90% of the comparisons are found to be in statistical agreement.

32 This initial study has the potential to be extended to a larger collection of GRUAN profiles, covering
33 multiple sites and years, with the aim of providing a robust estimation of both errors and
34 uncertainties of NWP model fields in radiance space for a selection of key microwave and infrared
35 frequencies.

36



37 1. Introduction

38 Space-borne observational datasets are EOS key-components that have led to significant advances in
39 climate and weather applications (Joo et al., 2013; Bauer et al., 2015; Hollmann et al., 2013; Bojinski
40 et al., 2014), and therefore must be subject to high standards of calibration and validation to meet
41 user requirements. As part of an overall strategy for a harmonised and improved instrument
42 calibration, the World Meteorological Organisation (WMO), Coordination Group for Meteorological
43 Satellite (CGMS), and Global Space-based Inter-Calibration System (GSICS) have advocated the need
44 to tie the measurements to absolute references and primary standards (WMO, 2011¹; GSICS, 2015²).
45 In most cases however, commonly used validation techniques, as discussed by Zeng et al. (2015) and
46 Loew et al. (2017), do not yet provide a full metrological traceability.

47 For a full metrological traceability and uncertainty quantification, Green et al (2018) suggested
48 mirroring the measurement protocols as described by Immler et al (2010). Accordingly, consistency
49 between two independent measurements, m_1 and m_2 , is achieved when:

$$|m_1 - m_2| < k \sqrt{\sigma^2 + u_1^2 + u_2^2} \quad (1)$$

50 where u_1 and u_2 are the total uncertainties associated with m_1 and m_2 , respectively. σ represents the
51 intrinsic uncertainties of the comparison. In the case of a comparison between radiosonde and
52 satellite observations for example, this term can represent the collocation uncertainty (Calbet et al.,
53 2017). k is a coverage factor expanding the confidence interval for normally distributed error
54 probability.

55

56 For satellite data, pre-launch calibration characteristics are often provided by the instrument
57 manufacturer or space agency. However at launch, an uncertainty chain that may have been
58 metrologically traceable during the laboratory calibration phase can become compromised due to
59 changes in the spacecraft during the launch process itself as well as changes in the satellite
60 environment in orbit compared to the laboratory testing. Furthermore, the instruments also degrade
61 over time, sometimes in quite a complex manner. These issues coupled with the current lack of true
62 on-board traceable references makes creating a metrologically traceable uncertainty chain difficult
63 for the satellite data record.

64 This aspect is being addressed by the Fidelity and Uncertainty in Climate Data Records from Space
65 (FIDUCEO) project (<http://www.fiduceo.eu/>). The project aims to develop Fundamental Climate Data
66 Records (FCDR) by reprocessing existing observations from raw satellite data to geolocated and
67 calibrated radiances with traceable uncertainties from a set of different references at the pixel level.
68 The uncertainty characterisation will account for the physical basis of the sensing process, the on-
69 board calibration system, and an estimate for the uncertainties arising from the processing.

¹ https://library.wmo.int/opac/doc_num.php?explnum_id=3710

² http://www.wmo.int/pages/prog/sat/documents/GSICS-RD002_Vision.pdf



70

71 The (re)assessment of historical, well-established, and new space-borne instruments using data
72 assimilation systems has become, over the past decade, common practice in numerical weather
73 prediction (NWP) centres (Bell et al., 2008; Zou et al., 2011; Bormann et al., 2013; Lu and Bell, 2014).
74 NWP models offer an interesting framework for the assessment of observational datasets due to a
75 physically constrained, continuous, global, and homogeneous representation of the atmosphere. An
76 optimal estimation of the state of the atmosphere is routinely performed in data assimilation
77 systems by blending information from a large volume of observations (space-borne, air-borne, and
78 ground-based) with a short-range forecast. Diagnostics are calculated in satellite observation space,
79 typically in brightness temperature, thanks to the radiative transfer models used by data assimilation
80 systems (Saunders et al., 2018). This forward approach is better posed than the inverse problem,
81 that is to say comparing model geophysical fields to retrieved satellite profiles, since multiple
82 atmospheric states can provide solutions to the retrieval, introducing further uncertainty. NWP
83 representation of atmospheric temperature and humidity fields is of sufficient quality to enable the
84 characterisation of subtle biases in satellite observations as demonstrated in the work referenced
85 herein. Loew et al. (2017) reported model fields uncertainties in the satellite observation space
86 ranging from 0.05 to 0.2K at frequencies principally sensitive to mid-tropospheric and lower
87 stratospheric temperature, and from 1 to 2K at frequencies sensitive to mid and upper tropospheric
88 humidity. However, those estimations arise from sensitivity studies and not from robust uncertainty
89 analyses. Stochastic approaches, based on ensemble forecasting techniques, have been used to
90 estimate forecast uncertainties, but with the caveat that they do not represent the systematic model
91 biases (Leutbecher et al., 2017).

92 This lack of metrologically traceable characterisation has often hampered the recognition and
93 consideration of model-based assessment outside of the NWP context, especially at space agency
94 and instrument team levels. Key climate users can also benefit from this approach, which has begun
95 to find resonance in the climate community (e.g. Massonnet et al., 2016).

96

97 In this paper, we use the terms *error* and *uncertainty* as described in the International Vocabulary of
98 Metrology (VIM) (JCGM, 2012³). The uncertainty is described in the VIM as a non-negative
99 parameter characterizing the dispersion of the quantity values being attributed to the quantity
100 intended to be measured, based on the information used. It is emphasized that all components of
101 the uncertainty contribute to this dispersion. This includes systematic effects arising from, for
102 example, corrections or reference standards. If a systematic effect is unknown it is unaccounted in
103 the uncertainty budget but contributes to the error.

104 The error is defined as the measured quantity value minus the unknown true value and may be
105 composed of a random and a systematic component.

106

107 The Gap Analysis for Integrated Atmospheric ECV CLimate Monitoring (GAIA-CLIM) project (Thorne
108 et al., 2017) aims to address those challenges by improving the use of in-situ observations to

³ <https://www.bipm.org/en/publications/guides/vim.html>



109 rigorously characterise a set of atmospheric Essential Climate Variables (ECVs) derived from satellite
110 observations as well as the geolocated and calibrated spectral radiances (level 1b) from which these
111 quantities are derived (<http://www.gaia-clim.eu/>). The work presented here is embedded in that
112 framework and focuses on developing NWP as a comprehensive reference by establishing
113 traceability for the model fields through comparison with traceable comparator data.

114 The NWP model error and uncertainty budget can be expressed as a function of four main
115 contributions:

- 116 a) The error and uncertainty in NWP temperature and humidity fields mapped to observation
117 space (brightness temperature).
- 118 b) The error and uncertainty in the underlying radiative transfer modelling, including biases
119 between fast radiative transfer models commonly used in NWP and reference line-by-line
120 models, fundamental spectroscopic uncertainty, and surface emissivity uncertainty.
- 121 c) The error and uncertainty due to scale mismatch. This encompasses the different scale at
122 which observation and model are resolved, and the scale of natural variability that is,
123 especially for humidity, much smaller than both observation and model scales.
- 124 d) The error and uncertainty due to residual cloud. Clear-sky scenes are generally preferred
125 because simulated cloudy radiances are affected by uncertainties in model representation of
126 cloud amounts and the absorption and scattering properties of hydrometeors.

127 This study aims to address the first contribution. To that end, the Met Office and European Centre
128 for Medium-range Weather Forecasts (ECMWF) models are compared to radiosondes from the
129 Global Climate Observing System (GCOS) Reference Upper-Air Network (GRUAN) in a stand-alone
130 module based on the core radiative transfer modelling capability of the fast radiative transfer model
131 RTTOV and the Radiance Simulator (both available on <http://www.nwpsaf.eu/>). This software,
132 referred to as the GRUAN Processor, enables the collocation of geophysical fields and simulation of
133 top-of-atmosphere (TOA) brightness temperatures (T_b) from radiosondes and NWP models, with
134 GRUAN uncertainties propagated into the radiative transfer calculation.

135

136 Section 2 introduces the datasets used for this study, namely GRUAN radiosondes and the NWP
137 models from the Met Office and ECMWF. Sections 3 and 4 describes the GRUAN Processor
138 functionality and presents an illustrative case study. A methodology statistically assessing the
139 uncertainties is presented in section 5. Section 6 concludes the study.

140

141 2. Datasets

142 2.1. GRUAN

143 With 17 sites across the world (including two inactive sites in the Pacific), GCOS is building on
144 existing infrastructures to develop a reference network for upper-air observations
145 (<http://www.gruan.org/>). GRUAN aims to provide long-term high-quality measurements of ECVs
146 with vertically resolved uncertainty estimates. To meet the strict criteria for reference
147 measurements, GRUAN data also includes a comprehensive collection of metadata and
148 documentation of correction algorithms.



149 To date, only the Vaisala RS92 radiosonde is used to produce the GRUAN certified products (Sommer
150 et al., 2016), referred to as RS92 GRUAN Data Product Version 2 (RS92-GDP), but a new product
151 based on the Vaisala RS41 is in preparation. The RS92 GRUAN processing is documented by Dirksen
152 et al (2014). This includes the correction of the radiosonde systematic errors, due to mainly solar
153 radiation, and the derivation of the uncertainties for temperature, humidity, wind, pressure, and
154 geopotential height. The total uncertainty budget accounts for correlated and uncorrelated
155 contributions of both random sources of uncertainty and uncertainties from systematic error
156 corrections, and it is expressed as the root sum square of all contributions. The uncertainty related
157 to the short wave radiation correction (used in the temperature uncertainty budget), the correlated
158 uncertainty related to systematic error corrections, and uncorrelated uncertainty (standard
159 deviation) derived from the GRUAN processing are available in the RS92-GDP files, in addition to the
160 total uncertainty of each variables. However, not all correlated and uncorrelated components are
161 independently available (albeit used in the calculation of the total uncertainty) and some sources of
162 partially correlated uncertainty are not yet modelled in GRUAN algorithms (e.g. the pendulum
163 motion of the radiosonde under the balloon). Therefore, only the total uncertainties of temperature,
164 humidity, and pressure are considered in this study.

165 The results presented in this preliminary study focus on the profiles from Lindenberg (LIN), GRUAN
166 lead centre, Germany (52.21°N, 14.12°E) for the year 2016.

167

168 2.2. Met Office NWP

169 Met Office model data files are extracted from the Managed Archive Storage System (MASS) and
170 only $\pm 5^\circ$ latitude and longitude around the GRUAN launch site is kept to limit the data volume. For
171 LIN, the model fields cover the area 47.109-57.109°N and 9.0234-19.102°E. Each model data file
172 contains four time steps starting at T+0, the analysis, and three successive 3-hour forecasts referred
173 to as T+3, T+6, and T+9. The Met Office data assimilation system is a hybrid 4-dimensional
174 variational analysis (4D-Var) with 6-hour time window (Lorenc et al., 2000; Rawlins et al., 2007). Four
175 analyses (and their successive forecasts) are available every day at 00:00, 06:00, 12:00, and 18:00
176 Coordinated Universal Time (UTC). Assimilated satellite radiances are corrected with a variational
177 bias correction similar to the scheme described by Auligné et al. (2007). The operational forecast
178 model in 2016 had a resolution of approximately 17km at mid-latitudes for 70 levels from surface to
179 80km (N768L70). The radiative transfer calculation was performed in 2016 by the fast radiative
180 transfer model RTTOV version 9 (Saunders et al., 1999, 2007).

181

182 2.3. ECMWF NWP

183 ECMWF data are extracted from the Meteorological Archival and Retrieval System (MARS⁴). Data
184 come from the operational data class atmospheric model long window 4Dvar stream (see MARS
185 documentation for details). The covered area is the same as for the Met Office. Each model data file
186 contains six time steps of three hours starting from T+0 to T+15. The ECMWF analysis/forecast

⁴ <https://software.ecmwf.int/wiki/display/UDOC/MARS+user+documentation>



187 system is documented by ECMWF⁵. A cubic octahedral reduced Gaussian grid is currently used with
188 a resolution of TCo1279 (horizontal grid spacing of about 9 km) and with 137 levels in the vertical.
189 Note that from February 2006 until June 2013, there were 91 vertical levels, and from January 2010
190 until March 2016 a linear reduced Gaussian grid was used with a horizontal spacing of around 16 km.
191 Data assimilation uses incremental 4D-Var (Courtier et al., 1994) with a 12-hour window, the
192 nominal 00:00 UTC analysis uses data from 21:00 UTC to 09:00 UTC. Forecasts and ensembles are
193 run twice daily from early-delivery 6-hour window 4D-Var analyses (Haseler, 2004). Flow-dependent
194 ensemble information from the ECMWF ensemble of data assimilations is incorporated into the
195 modelling of background-error covariances (Bonavita et al., 2016). Satellite radiative transfer
196 calculations use the fast radiative transfer model RTTOV version 11.2 (Hocking et al., 2015) has been
197 used operationally since May 2015 (Lupu and Geer, 2015). Variational bias correction of satellite
198 radiances (and aircraft temperatures) is based on Dee (2004) and Auligné et al (2007).

199

200 3. Processor design

201 The GRUAN Processor, a software based on the NWP Satellite Application Facility (SAF) Radiance
202 Simulator (Smith, 2017), is designed to collocate NWP model fields from the Met Office or ECMWF
203 with radiosondes from the GRUAN network and simulate TOA Tb from those collocated profiles. The
204 simulations are performed at frequencies used by meteorological space-borne instruments and
205 supported by RTTOV. Figure 1 illustrates the Processor top-level design with its main processing
206 steps.

207

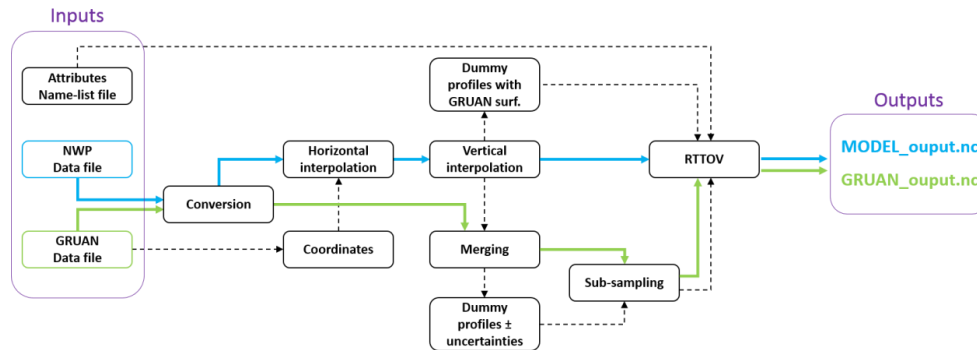
208 3.1. Inputs

209 The Processor requires as input a GRUAN and a model data file. Supported products are GRUAN
210 RS92-GDP, Met Office Unified Model (UM) Fieldfiles (or PP files, see Smith (2017)), and ECMWF GRIB
211 files. Both model file types must contain the minimum set of required variables as described by
212 Smith (2017) for the Radiance Simulator. Processing options and RTTOV attributes are provided via a
213 text file read by the Processor. This file includes the instrument characteristics (e.g. channels) to be
214 simulated and output options (output in unit of radiances or Tb for example). Optionally, RTTOV bias
215 and root mean square error (rmse) estimated from comparisons between RTTOV and line-by-line
216 model calculations, as provided by NWP SAF⁶, can be written to the output files. Finally, an option
217 allows to opt for a model-radiosonde collocation following the balloon drift (in space and time, see
218 section 3.3) or assuming no drift. Note that all collocations presented in this paper account for the
219 radiosonde drift.

220

⁵ <https://www.ecmwf.int/en/forecasts/documentation-and-support>

⁶ <https://www.nwpsaf.eu/site/software/rttov/download/coefficients/comparison-with-lbl-simulations/>



221

222 Figure1: GRUAN Processor top-level design. Solid arrows show the main processing steps from input
 223 (blue for NWP model data and green for GRUAN data) to output. Dashed arrows represent the
 224 internal processing.

225

226 3.2. Conversion

227 The conversion step ensures that both model and GRUAN variables (e.g. temperature or humidity)
 228 are expressed in the same units and that those units are compatible with RTTOV (see section 3.5).
 229 Two main types of conversion are supported: temperature from potential temperature and specific
 230 humidity from relative humidity.

231

232 Model data files may sometimes contain potential temperature instead of temperature profiles, as is
 233 the case for the Met Office. Temperature (T) is therefore calculated as a function of potential
 234 temperature (θ) and pressure (P) as follows:

$$T = \theta \left(\frac{P}{P_0} \right)^\kappa \quad (2)$$

235

236 where P_0 is the standard reference pressure equal to 1000hPa and κ the ratio of the gas constant of
 237 air to the specific heat capacity at constant pressure.

238 Similarly, it is worth noting that model data files may not directly contain pressure profiles (e.g. in
 239 ECMWF files) or the pressure may be expressed on a different set of levels with respect to other
 240 variables (e.g. Met Office files). In both cases however, the pressure on model levels can be
 241 calculated from coefficients provided in the model data files.

242

243 The expression of humidity also needs to be harmonised. GRUAN provides profiles of relative
 244 humidity (RH), whereas the humidity from both NWP models is expressed in specific humidity (q), in
 245 units kg.kg^{-1} . GRUAN RH is converted to q as follows:



$$q = \frac{\varepsilon RH e_s}{(P - (1 - \varepsilon) RH e_s)} \quad (3)$$

246

247 where ε is the ratio of the molecular weight of water vapour to the molecular weight of dry air and
248 e_s the saturation vapour pressure over liquid. For consistency with GRUAN and Vaisala processing, e_s
249 is expressed as defined by Hyland and Wexler (1983), such that:

$$\ln(e_s) = \frac{C_1}{T} + C_2 + C_3 T + C_4 T^2 + C_5 T^3 + C_6 \ln(T) \quad (4)$$

250

251 with:

$$252 \quad C_1 = -5.8002206 \times 10^3$$

$$253 \quad C_2 = 1.3914993 \times 10^0$$

$$254 \quad C_3 = -4.8640239 \times 10^{-2}$$

$$255 \quad C_4 = 4.1764768 \times 10^{-5}$$

$$256 \quad C_5 = -1.4452093 \times 10^{-8}$$

$$257 \quad C_6 = 6.5459673 \times 10^0$$

258 for e_s in Pa and T in K.

259

260 3.3. Interpolations

261 The GRUAN Processor generates a set of model profiles (i.e. one profile per variable), on model
262 levels, interpolated in space and time along the radiosonde path, which are then vertically
263 interpolated on a fixed set of 278 levels as follows.

264 First, model fields are linearly interpolated at the radiosonde coordinates (latitude-longitude-time),
265 weighted by the distance to the eight closest grid points. Therefore, for an observation at the
266 coordinate $p=[x_p, y_p, z_p]$, as illustrated on figure 2, in a cube of vertices $[(x,y,z), (x+dx,y,z), (x,y+dy,z),$
267 $(x,y,z+dz), (x+dx,y+dy,z), (x+dx,y,z+dz), (x,y+dy,z+dz), (x+dx,y+dy,z+dz)]$, where dx and dy represent
268 the grid point interval in latitude and longitude, respectively, and dz the interval between the time
269 $T+n$ and $T+(n+1)$, with associated field values F_p and $[F_{000}, F_{100}, F_{010}, F_{001}, F_{110}, F_{101}, F_{011}, F_{111}]$,
270 respectively, F_p is calculated as follows:



$$\begin{aligned}
 F_p = & F_{000}(1 - w_x)(1 - w_y)(1 - w_z) \\
 & + F_{100}w_x(1 - w_y)(1 - w_z) \\
 & + F_{010}(1 - w_x)w_y(1 - w_z) \\
 & + F_{001}(1 - w_x)(1 - w_y)w_z \\
 & + F_{101}w_x(1 - w_y)w_z \\
 & + F_{011}(1 - w_x)w_yw_z \\
 & + F_{110}w_xw_y(1 - w_z) \\
 & + F_{111}w_xw_yw_z
 \end{aligned}
 \tag{5}$$

271

272 where w_x , w_y , and w_z are the weights defined as:

$$w_x = (x_p - x)/dx \tag{6}$$

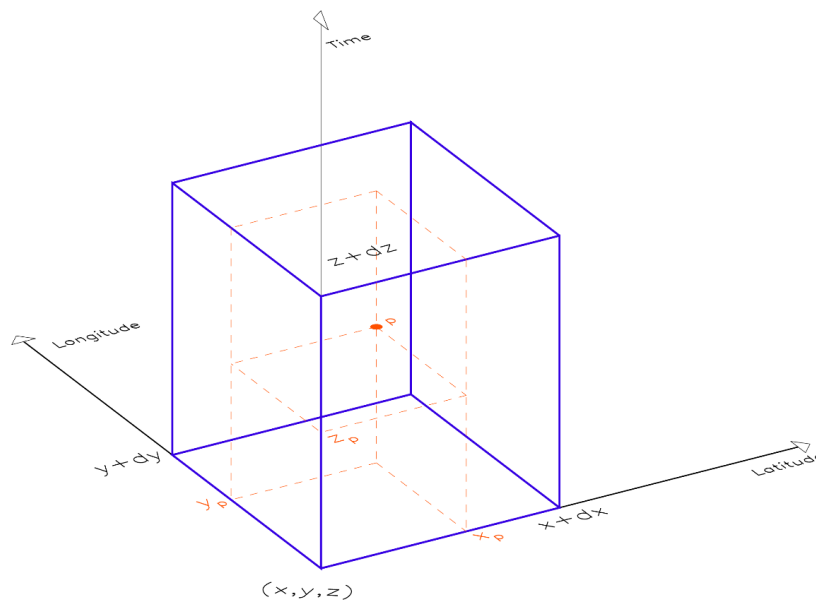
$$w_y = (y_p - y)/dy \tag{7}$$

$$w_z = (z_p - z)/dz \tag{8}$$

273

274 This operation is repeated along the radiosonde path with a time-step of 15 seconds based on the
 275 radiosonde time profile. A unique model profile (one for each variable) is reconstructed by
 276 combining the model fields from the pressure levels crossed by the radiosonde between two
 277 consecutive interpolated model profiles.

278



279

280 Figure 2: illustration of an observation of coordinate (x_p, y_p, z_p) in a cube that vertices represent the
 281 model latitude (x axis), longitude (y axis), and forecast time (z axis).

282



283 The reconstructed set of profiles is then interpolated on a fixed vertical grid of 278 pressure levels.
 284 The fixed grid, referred to as Processor grid (Pg), has been designed to have at least one Pg level
 285 between any two levels of the coarser model (Met Office or ECMWF) grid, referred to as Coarse grid
 286 (Cg). Therefore, for Pg of dimension n equal to 278 and Cg of dimension m (equal to 70 for the Met
 287 Office, 91 or 137 for ECMWF), the interpolation is calculated by weighting the fields with respect to
 288 the pressure via the interpolation matrix W of dimension $n \times m$, such as:

$$Pg = W Cg \quad (9)$$

289

290 where for the j^{th} pressure (P) level of Pg located between the i^{th} and $i+1^{\text{th}}$ levels of Cg :

$$Pg_j = W_{j1} Cg_1 + W_{j2} Cg_2 + \dots + W_{jm} Cg_m \quad (10)$$

$$W_{ji} = \frac{P_{i+1} - P_j}{P_{i+1} - P_i} \quad (11)$$

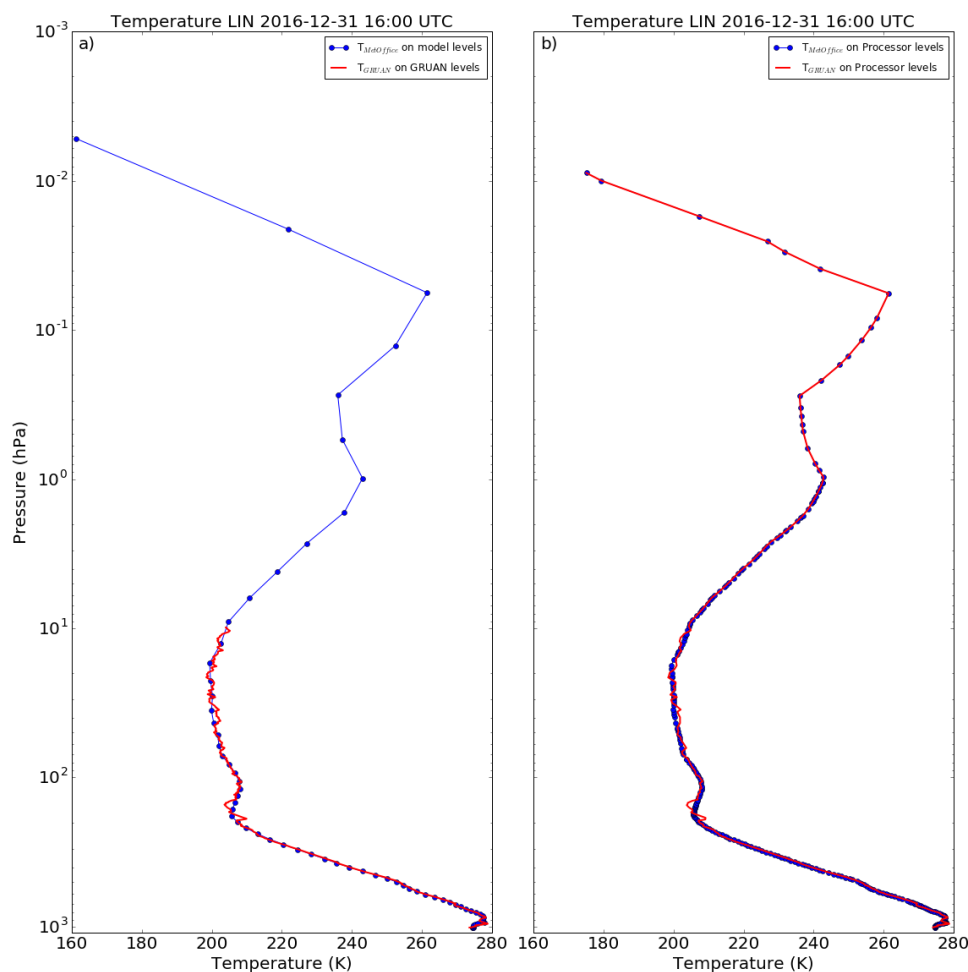
$$W_{ji+1} = 1 - W_{ji} \quad (12)$$

$$W_{jk} = 0 \text{ where } k \neq i, i + 1 \quad (13)$$

291

292 The vertical interpolation of model profiles as well as the subsampling of the radiosonde profiles
 293 (see section 3.4) to the Processor grid aims to provide a homogenised number of vertical levels on
 294 which the radiative transfer equation is calculated. Although the coarse model grid and the fine
 295 radiosonde grid could be directly used as input in RTTOV, it was observed that the lack of
 296 homogenisation between model and radiosonde profiles causes a bias in radiance space. It was
 297 therefore decided to interpolate the model profiles and provide a way to estimate the uncertainty
 298 associated to this interpolation (see section 5).

299 Figure 3 illustrates the change from a collocated Met Office temperature profile (LIN 31 December
 300 2016, 16:00 UTC) on model levels (70 levels) (a) to a collocated Met Office profile interpolated on
 301 the Processor grid (278 levels) (b).



302

303 Figure 3: (a) GRUAN temperature profile (red line) from Lindenberg on 31 December 2016, 16:00
304 UTC as provided in the RS92-GDP data file with full GRUAN vertical resolution and collocated Met
305 Office temperature profile (blue dotted line) on the model vertical levels. (b) GRUAN temperature
306 profile subsampled at the Processor 278 pressure levels and merged with the Met Office profile
307 above 9.8 hPa (red line) and collocated Met Office temperature profile interpolated on the Processor
308 vertical levels (blue dotted line).

309

310 3.4. Merging and subsampling

311 A caveat of processing radiosonde profiles in RTTOV is the lack of information between the top of a
312 profile (bursting point of the balloon) and the TOA. This is addressed by merging the radiosonde
313 profiles with the model profiles above the last available point of the radiosonde. Note that this step
314 occurs after the interpolation of the model profiles so that the upper merged part of the radiosonde
315 and model profiles are strictly identical.



316 Similarly, RTTOV requires surfaces information: 2m temperature and humidity, surface pressure and
317 altitude, 10m wind (u and v components, used for microwave simulations over ocean), and skin
318 temperature. While GRUAN provides the surface pressure, temperature, relative humidity, and
319 altitude at launch site in all the data files, the skin temperature (T_{skin}^G) has to be derived from the
320 difference between the model skin (T_{skin}^M) and the 2m temperature (T_{2m}^M) applied to the GRUAN
321 surface temperature (T_{2m}^G) such as:

$$T_{skin}^G = T_{2m}^G + (T_{skin}^M - T_{2m}^M) \quad (14)$$

322

323 Although the 10m wind could be provided by the Vaisala wind profiles (available in GRUAN data
324 files) or calculated from GRUAN profiles of wind speed and direction, the chaotic rotation of the
325 radiosonde just after launch results in unreliable wind information near the surface. Therefore, the
326 model 10m wind (u and v components) is also merged with the GRUAN data. Note that 10m wind is
327 used to calculate the sea surface emissivity (for microwave simulations) and therefore only concerns
328 GRUAN sites on small island sites (i.e. La Reunion, Nauru, Manau, Ny-Ålesund, Graciosa, and
329 Tenerife).

330

331 In the raw RS92 data and GRUAN data, the samplings are provided every second but filtering reduces
332 the effective resolution of temperature to approximately 10s at low levels; the effective resolution
333 of humidity is similar but it is reduced to 40-50s at upper levels (Dirksen et al., 2014). As a result,
334 GRUAN profiles count several thousand levels in the vertical that need to be reduced to the number
335 of levels on the Processor grid. This is achieved with a subsampling of the radiosonde profiles to the
336 nearest levels for each of the 278 Processor pressure levels, at levels where data are available, with
337 the imposed constraint that the ratio radiosonde pressure by Processor pressure must be less than
338 0.1%.

339 The subsampling of GRUAN profiles has been preferred over layer-averaging or convolution
340 techniques for several reasons. First, we aimed to avoid all unnecessary modification of the GRUAN
341 profiles, used as reference in this study. Second, GRUAN uncertainties are vertically resolved and
342 their processing would have resulted in an information loss. Third, the aim of the Processor is to
343 evaluate uncertainties in radiance space. During the testing phase, we observed that neither the
344 choice of averaged layers nor sub-sampled levels significantly affects the calculation of radiative
345 transfer and the resulting brightness temperatures.

346 Fig. 3 shows a the changes from a GRUAN temperature profile (LIN 31 December 2016, 16:00 UTC)
347 as provided in the RS92-GDP data file (5821 levels, from the surface to 9.88 hPa) (a) to a Processor
348 merged and subsampled profile (278 levels, from the surface to 0.008 hPa) (b).

349

350 3.5. RTTOV and uncertainties

351 The radiosonde and model profiles, both on the Processor vertical grid, and their respective surface
352 parameters are passed to RTTOV for the calculation of the TOA Tb. RTTOV version 11.3, currently
353 used by the GRUAN Processor, is documented by Hocking et al. (2015).



354 The surface emissivity depends on the surface type. For land and sea ice, the Processor uses a fixed
355 value, 0.95 and 0.92, respectively. Those estimates are potentially far from the truth, but any bias
356 introduced by fixed emissivity terms is expected to cancel out when the difference in simulated T_b is
357 calculated. Note that RTTOV allows the use of the emissivity atlases over land and sea ice, but this
358 option has not yet been investigated. Over sea, the surface emissivity is calculated by the RTTOV
359 FAST Emissivity Model (FASTEM) version 5 (Kazumori and English, 2015). Although the version 5 is
360 the default version, this can be changed in the input attribute file. It is worth noting here that
361 although the radiosonde may drift from above land to above sea (ice) (or the opposite), the surface
362 type can only be of one kind. The land surface type is typically used as most radiosonde launch sites
363 are well inside land masses. However, for the small island sites of La Reunion, Nauru, Manau, Ny-
364 Ålesund, Graciosa, and Tenerife, the radiosonde is expected to rapidly drift over sea and therefore
365 the sea surface type is used instead. The difference between sea and sea ice is controlled by the sea-
366 ice mask used by the NWP model.

367 The viewing angle is set by default to nadir (0°) for all simulations. However, different angles could
368 potentially be used for the purpose of better comparisons with real satellite data, for example.

369 All simulations assume clear sky scenes and uses RTTOV direct mode (ignoring the scattering) with
370 the cloud liquid water option off (data not available from GRUAN data file). It is acknowledged that
371 this may introduce discrepancies in the comparison between model and radiosonde in situations
372 where the radiosonde encounters one or several cloud layers. The brightness temperatures
373 calculated from the radiosonde data perturbed by the presence of clouds (e.g. peaks in the humidity
374 profile and to a lesser extent in the temperature profile) will differ from those calculated from the
375 model data that assume clear sky conditions. Because the RS92-GDP does not provide a cloud flag,
376 indirect screening may be required for fine comparisons. To that end, one can use the precipitable
377 water column from the RS92-GDP metadata as a proxy for cloud and or assume the presence of
378 cloud when the relative humidity exceeds a threshold value.

379 Finally, note that RTTOV interpolation mode (used to interpolate the input levels to the coefficient
380 levels for the calculation of the atmospheric optical depth, and then back from the coefficient levels
381 to the input levels for the calculation of the radiative transfer equation) uses the log-linear on
382 weighting function mode as described by Hocking et al. (2015). This is aimed to avoid a known issue
383 causing the oscillation of the temperature Jacobians.

384

385 It was observed that the interpolation of the model fields at the GRUAN launch site coordinates
386 results in large discrepancies, especially affecting surface parameters (surface pressure and
387 elevation) and the lower part of the profiles, when the local orography presents large variations at
388 scales of the same order as the model grid resolution. The interpolation, using the weighted average
389 of the four neighbouring grid points at a given forecast time may result in the model surface being
390 below or above the actual GRUAN launch site surface. A typical example is the site at La Réunion
391 where the radiosondes are launched from the Maïdo observatory at an altitude of 2200m, compared
392 to which the interpolation of the ECMWF model gives an altitude of 980m and the interpolation of
393 the Met Office model 0m. In Lindenberg by comparison, the radiosondes are launched from the
394 altitude of 103m while both models estimates the altitude to be 57m. To estimate the associated
395 error, a set of dummy model profiles are generated with the surface pressure forced to that



396 provided in the GRUAN metadata. If the model has a surface below that of the observations, the
397 model profiles are linearly interpolated and cut at the observed surface pressure, and the surface
398 parameters become those of the lowest level. If the model has a surface above that of the
399 observations, the model profiles are linearly extrapolated to the observed surface pressure, and the
400 model surface parameters become those of the new lowest level. The difference between the T_b
401 calculated from those modified profiles and the T_b calculated from the original profiles provides an
402 estimation of the associated error. This is referred to as u_{surf_bt} in the Processor output.

403

404 Finally, the GRUAN uncertainties are propagated into radiance space. As described by Calbet et al.
405 (2017), this can be achieved by multiplying the GRUAN profiles of uncertainty by the Jacobians
406 derived by RTTOV from the GRUAN atmospheric profiles, or by applying the radiative transfer to the
407 input atmospheric GRUAN profiles perturbed with their associated uncertainties. The GRUAN
408 Processor is designed to follow the second method although the first one will be further discussed in
409 section 5. In the Processor, two sets of perturbed profiles are created, one containing the GRUAN
410 profiles of temperature, pressure, and humidity, incremented by their respective total uncertainty
411 ($T+u_{temp}$, $P+u_{press}$, and $q+u_q$), and one containing the GRUAN profiles decremented by their
412 total uncertainty ($T-u_{temp}$, $P-u_{press}$, and $q-u_q$). The resulting brightness temperatures
413 calculated by RTTOV based on those two sets of perturbed profiles, referred to as T_b^+ and T_b^- ,
414 respectively, are compared to T_b , calculated with the unperturbed profiles, to estimate the
415 associated uncertainty in radiance space. The greatest difference between $|T_b - T_b^+|$ and $|T_b - T_b^-|$
416 is given in output as u_{gruan_bt} . Note that all eight possible combinations of sign have been tried
417 during the test phase. The resulting uncertainty was not found significantly different from that
418 obtained with T_b^+ or T_b^- , but the processing time significantly increase. T_b^+ and T_b^- were therefore
419 retained as the best compromise.

420 This approach assumes that the GRUAN profiles of uncertainty used to perturb the atmospheric
421 profiles are fully correlated at all levels. This assumption differs from the truth in that GRUAN total
422 uncertainty consist of a root sum square of correlated and uncorrelated components (Dirksen et al.,
423 2014). Nevertheless, assuming a fully correlated perturbation allows the estimation of the total
424 GRUAN uncertainty upper bound in radiance space. The lower bound, not addressed in the GRUAN
425 Processor, can be obtained by assuming the uncertainty profiles completely uncorrelated, and lies
426 close to zero as demonstrated by Calbet et al. (2017).

427 Ideally, the correlated and uncorrelated components of GRUAN uncertainty should be treated
428 separately with, for example, the Monte Carlo method described in the Guide to the expression of
429 Uncertainty in Measurement (GUM) (JCGM, 2008⁷). However, those components are not all
430 independently available and it is currently not possible to differentiate them in the RS92-GDP. Note
431 that the radiosonde (random and/or systematic) errors are not provided. Instead, GRUAN algorithm
432 corrects the systematic errors in the radiosonde measurements, acknowledging that the correction
433 is not perfect and introduces an associated residual uncertainty (accounted for in the total
434 uncertainty).

⁷ <https://www.bipm.org/en/publications/guides/gum.html>



435 For completeness, perturbations to the surface parameters could be added to the total uncertainty
436 budget in radiance space, but GRUAN does not provide uncertainties associated with these
437 measurements. An alternative is discussed in section 5.

438

439 3.6. Outputs

440 For each pair of collocated radiosonde and NWP model fields, the GRUAN Processor generates two
441 outputs files in netcdf format. The first file contains the model-related fields including, but not
442 limited to, the profiles of temperature, humidity, and pressure on the Processor vertical grid, the
443 interpolation matrix W , the simulated brightness temperature, the temperature, humidity, and
444 pressure Jacobians, and a quality control flag (qcflags). Note that for successful simulations, qcflags is
445 equal to zero. The second file contains the GRUAN-related fields, including e.g. GRUAN atmospheric
446 profiles and associated uncertainties on the Processor vertical grid, the Jacobians, and the T_b and T_b
447 uncertainties estimated from the perturbed GRUAN profiles (u_gruan_bt).

448 Both files also contain metadata documenting the GRUAN Processor version number (here 6.2); the
449 NWP model, model validity time, and model version number; the simulated satellite name, platform,
450 and channel; the RTTOV version, RTTOV coefficients creation date, and bias and root mean square
451 error (when available); and the metadata available from the original RS92-GDP.

452

453 Note that some GRUAN Processor simulated brightness temperatures have been ingested into the
454 GAIA-CLIM Virtual Observatory (<http://gaia-clim.vo.eumetsat.int/>) for the purposes of visualisation,
455 manipulation, and extraction of collocated GRUAN-NWP-Satellite data.

456

457 4. Data analysis illustration

458 For illustration purposes, one year of collocated profiles and simulated T_b is presented. The dataset
459 corresponds to 1160 radiosondes launched from Lindenberg, Germany, in 2016, compared to the
460 Met Office and ECMWF models. T_b values have been simulated at the Advanced Technology
461 Microwave Sounder (ATMS) 22 channel frequencies, a microwave radiometer with sounding
462 capability in the oxygen band (53-57GHz), sensitive to tropospheric and lower stratospheric
463 temperature, and in the water vapour band (around 183GHz), sensitive to mid-to-upper
464 tropospheric humidity (Bormann et al., 2013).

465 The dataset is divided into two samples composed of day and night-time profiles, respectively. This
466 is aimed at discriminating the GRUAN profiles affected by solar radiation, the dominant source of
467 uncertainty according to Dirksen et al. (2014). All profiles with a solar zenith angle (calculated as a
468 function of latitude, longitude, and UTC) smaller (greater) than 90° at launch time is considered as
469 day (night) time. Note that for a refined analysis, the whole profile (not just launch time) should be
470 checked and only profiles with the sun below (or above) the horizon throughout should be used.

471 Note that no cloud screening is applied in this study.



472 After screening, 573 pairs of GRUAN Processor outputs are available in daytime and 587 in night-
473 time for each model. The mean difference $NWP - GRUAN$ in temperature, humidity, and simulated
474 T_b is shown in figures 4 (daytime) and 5 (night-time) together with the number of available
475 comparisons as a function of the pressure. Note that at pressures less than 10hPa, the data sampling
476 decreases rapidly as less balloons reach those levels. An arithmetic mean is used to average the
477 uncertainty over the sampling according to Immler et al. (2010) Eq. (4). For temperature and
478 humidity, the GRUAN total uncertainty as provided in the RS92-GDP is used (the relative humidity
479 uncertainty is converted into specific humidity uncertainty in the GRUAN Processor), while the
480 uncertainty in T_b shows the GRUAN uncertainties propagated in radiance space via the perturbation
481 of the atmospheric profiles. Note that the model uncertainty and the uncertainty associated with
482 the vertical interpolation are ignored in this section, but addressed in section 5.

483 It is important to note that both Met Office and ECMWF are operationally assimilating the
484 radiosonde profiles from the GCOS Upper Air Network (GUAN), which, in Lindenberg, are the same
485 as the GRUAN profiles but without the specific GRUAN processing (and without uncertainty
486 characterisation). Therefore, unlike the forecasts, the model analyses (T+0) are not completely
487 independent from the observations. However, this is not expected to affect significantly the mean
488 comparison as only about 5% of the profiles fall in the first time window (i.e. interpolation between
489 T+0 and T+3).

490

491 In Figs 4 and 5, the main feature for ECMWF is a 0.5K cold bias in the stratosphere (100-10hPa),
492 observed both day and night. The model also presents a 50-75% wet bias peaking between 200 and
493 100hPa, slightly more pronounced during the day. This is consistent with the results from Ingleby
494 (2017) who showed a similar behaviour for several kinds of radiosonde.

495 The Met Office model presents a persistent 0.2 to 0.5K cold bias at pressure greater than 300hPa
496 and a 0.25K warm bias between 200 and 100hPa seen at night-time only. This is consistent with
497 Ingleby and Edwards (2015) who showed similar features in the comparison between radiosondes
498 and the Met Office regional model covering the United Kingdom. The Met Office tropospheric
499 humidity fits generally the radiosonde profiles well but presents a 50-60% wet bias with a peculiar
500 double peak at 200 and 100hPa. A wet bias peaking at 300hPa was already observed by Ingleby et al.
501 (2013), the coarser vertical resolution used by the authors potentially explaining the different
502 pressure level at which the bias is observed. However, the second maximum (at 100hPa) seems to
503 be a new feature that appears in 2015 and persists in 2017 (not shown). This remains unexplained to
504 date.

505 In radiance space, it is important to distinguish between frequencies representative of the difference
506 $NWP - GRUAN$ and those significantly affected by the surface and the mid to upper stratosphere
507 where the GRUAN profiles are merged with the model. Hence, ATMS frequencies sensitive to the
508 surface (23.8-54.4 and 88.2-165.5GHz, channel 1-7 and 16-17, respectively) and to the upper
509 stratosphere ($57.29 \pm 0.3222 \pm 0.022 - 57.29 \pm 0.3222 \pm 0.0045$ GHz, channel 13-15, respectively) should be
510 considered with caution and not used for scientific applications. On the contrary, frequencies
511 sensitive to the upper tropospheric-lower stratospheric temperature (peaking between 300 and
512 20hPa) and to the mid tropospheric humidity (peaking between 650 and 350hPa) cover the same



513 vertical domain as the information provided by GRUAN. For those frequencies, ATMS channel
 514 characteristics and mean Tb difference are provided in Table 1.

515

516 Table 1: Mean difference *NWP* – *GRUAN* in simulated Tb for ECMWF ($\Delta T_{b_{ECMWF}}$) and Met Office
 517 ($\Delta T_{b_{MetOffice}}$) and 1σ standard deviation for ATMS channels 8-12 and 18-22 at day and night-time.

Channel	Frequency (GHz)	$\Delta T_{b_{ECMWF}} (1\sigma)$ (K)		$\Delta T_{b_{MetOffice}} (1\sigma)$ (K)	
		night	day	night	day
8	54.94	-0.08 (0.09)	-0.16 (0.10)	-0.00 (0.11)	-0.04 (0.12)
9	55.5	-0.15 (0.12)	-0.24 (0.13)	0.04 (0.13)	-0.02 (0.14)
10	57.29	-0.32 (0.18)	-0.45 (0.18)	0.01 (0.16)	-0.07 (0.20)
11	57.29±0.217	-0.39 (0.21)	-0.54 (0.22)	-0.04 (0.20)	-0.16 (0.25)
12	57.29±0.3222±0.048	-0.34 (0.25)	-0.53 (0.27)	-0.09 (0.28)	-0.26 (0.31)
18	183.31±7.0	0.35 (0.91)	0.25 (1.09)	0.02 (0.83)	-0.36 (1.02)
19	183.31±7.0	0.37 (1.13)	0.15 (1.24)	-0.09 (1.03)	-0.48 (1.14)
20	183.31±3.0	0.34 (1.31)	-0.01 (1.36)	-0.18 (1.22)	-0.61 (1.27)
21	183.31±1.8	0.22 (1.48)	-0.29 (1.50)	-0.31 (1.42)	-0.81 (1.45)
22	183.31±1.0	0.04 (1.61)	-0.61 (1.64)	-0.46 (1.57)	-1.01 (1.60)

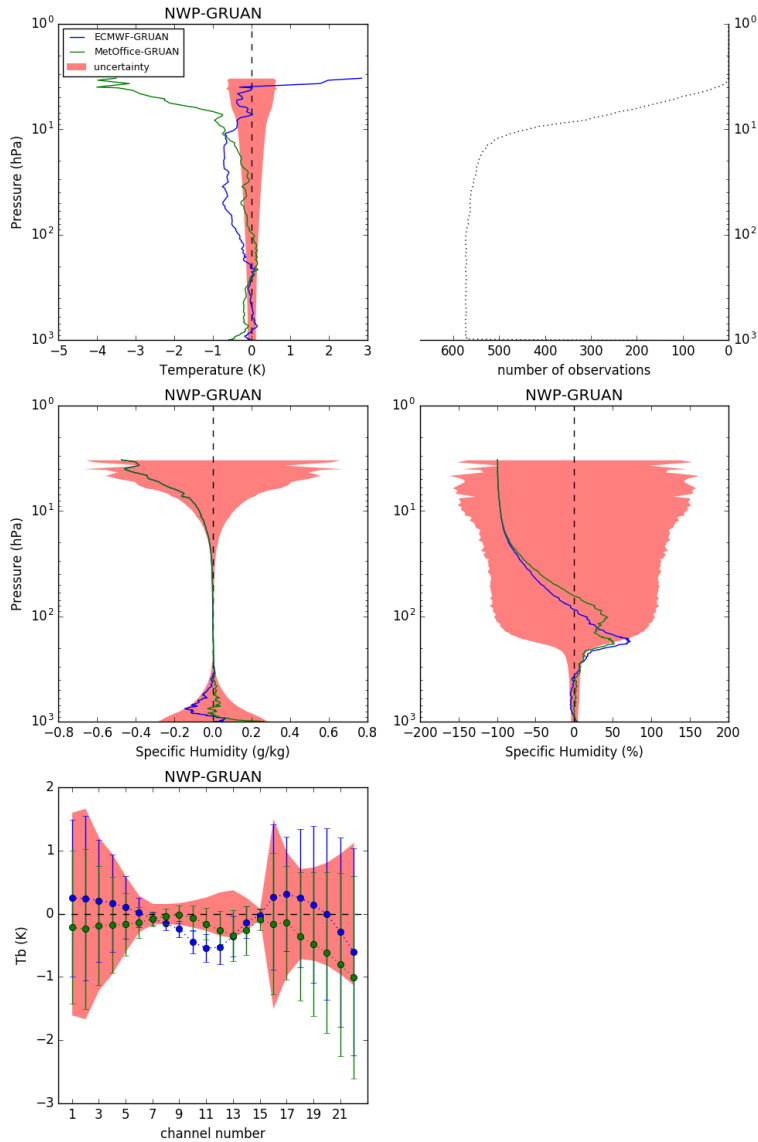
518

519 At frequencies sensitive to temperature (54-57GHz, channels 8-12), hereafter referred to as
 520 temperature channels, the mean difference for ECMWF varies from -0.08 to -0.39K at night, mostly
 521 outside GRUAN uncertainty (red shading, Fig. 5), reflecting the cold bias observed in the
 522 stratosphere. Note that a difference greater than GRUAN uncertainty does not mean a statistical
 523 disagreement since the uncertainty related to the model is unaccounted for (i.e. the total
 524 uncertainty of the comparison as expressed in Eq. (1) is larger than the GRUAN uncertainty alone).
 525 The difference is slightly larger in daytime (-0.16 to -0.54K). Similarly, the difference at frequencies
 526 sensitive to humidity (around 183GHz, channels 18-22), hereafter referred to as humidity channels,
 527 varies from 0.04 to 0.37K at night (-0.01 to -0.61K during the day), within GRUAN uncertainty.

528 The mean difference in Tb for the Met Office is always found within GRUAN uncertainty and varies
 529 from -0.09 to 0.04K during the night (-0.02 to -0.26K in daytime) for the temperature channels and
 530 from -0.46 to 0.02K during the night (-0.36 to -1.01K in daytime) for the humidity channels.

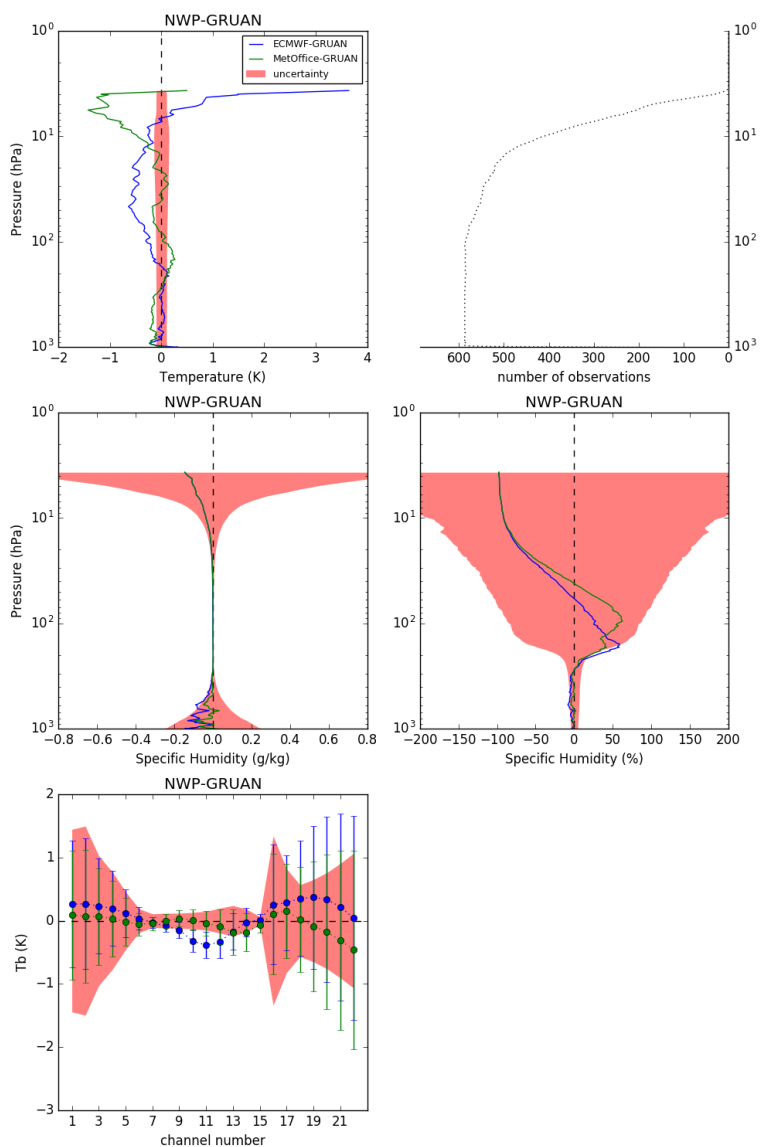
531 The standard deviation of the differences is similar for both centres and does not vary much from
 532 day to night.

533



534

535 Figure 4: Mean difference ECMWF – GRUAN (blue) and Met Office – GRUAN (green) calculated from
 536 573 daytime collocation from Lindenberg in 2016. The temperature difference (top left) is expressed
 537 in K, the humidity difference is expressed in g.kg^{-1} (middle left) and in percentage ($\frac{\text{NWP} - \text{GRUAN}}$
 538 / GRUAN) (middle right), and the difference in simulated brightness temperatures for ATMS
 539 channels is expressed in K (bottom) with the 1σ standard deviation (vertical bars). The red shading
 540 shows GRUAN uncertainty. The number of observations is shown as a function of the pressure (top
 541 right).



542

543 Figure 5: Same as figure 4 but for the 587 night-time collocations.

544

545 5. Comparison assessment

546 The previous section gives insights into the GRUAN uncertainty propagated in radiance space by the
 547 GRUAN Processor. The approach offers a rapid but incomplete evaluation of the *NWP – GRUAN*
 548 comparison, but several aspects are overlooked in the final budget, that for various reasons are not
 549 part of the internal Processor processing. This includes: a) the uncertainty associated with surface



550 parameters, not provided in RS92-GDP and likely to change from station to station, b) the NWP
 551 model uncertainty, often expressed as a covariance matrix and used in the data assimilation process
 552 by the NWP centres, but not available in the input data files, and c) the uncertainty associated with
 553 the vertical interpolation operated by the Processor for which estimation requires information on
 554 the last two points.

555 In this section, a mathematical framework is elaborated to estimate a robust uncertainty budget for
 556 the comparison between NWP fields and GRUAN observations, in radiance space, and statistically
 557 assess this comparison. This includes uncertainties in the GRUAN observations, in the vertical
 558 interpolation of the GRUAN Processor, and in the model fields. Note that, as previously mentioned,
 559 any comparison to satellite radiances should also include other sources of uncertainty such as in the
 560 underlying radiative transfer models and cloud detection. For this study, we focus on the
 561 comparison to the Met Office model fields, but the same method could be applied to the
 562 comparison with ECMWF fields.

563

564 We define \mathbf{x}_{rs} as the radiosonde profiles and \mathbf{x}_m as the model profiles (temperature, humidity, and
 565 pressure, with a pressure coordinate). Note that \mathbf{x}_{rs} and \mathbf{x}_m are on different vertical grids. \mathbf{x}_{rs} is on
 566 the GRUAN Processor vertical grid, composed of 278 levels, hereafter referred to as the fine grid (f),
 567 subsampled from the original GRUAN profiles (noting that with a ratio radiosonde pressure by
 568 Processor pressure less than 0.1%, the subsampling uncertainty is assumed negligible). \mathbf{x}_m is on the
 569 model vertical grid, hereafter referred to as the coarse grid (c), as given in input.

570 Given H , the observation operator, we can express the simulated Tb as follows:

$$\mathbf{y}_{rs} \equiv H(\mathbf{x}_{rs}) \quad (15)$$

$$\mathbf{y}_m \equiv H(\mathbf{W}\mathbf{x}_m) \quad (16)$$

571 where \mathbf{W} is the interpolation matrix.

572 Eq.s (15) and (16) can be further expanded as a function of the profiles true value on the fine and
 573 coarse grid, hereafter \mathbf{x}_f^t and \mathbf{x}_c^t , respectively, and the errors associated with the radiosonde and the
 574 model fields, hereafter $\boldsymbol{\varepsilon}_{rs}$ and $\boldsymbol{\varepsilon}_m$, as follows:

$$\mathbf{y}_{rs} = H(\mathbf{x}_f^t + \boldsymbol{\varepsilon}_{rs}) \quad (17)$$

$$\mathbf{y}_m = H(\mathbf{W}\mathbf{x}_c^t + \mathbf{W}\boldsymbol{\varepsilon}_m) \quad (18)$$

575 with \mathbf{x}_c^t defined as $\mathbf{x}_c^t \equiv \mathbf{W}^* \mathbf{x}_f^t$ where an expression for \mathbf{W}^* , the pseudo-inverse of \mathbf{W} , is given in
 576 Appendix B.

577 The comparison carried out in this study is in radiance space and the observation operator used to
 578 simulate the brightness temperatures is identical for both radiosonde and model fields simulations.
 579 For this reasons, we consider the radiance space as our reference and ignore any errors associated
 580 with observation operator, that would cancel out in the difference anyway since mainly systematic.
 581 Note that those errors need however to be taken into account if a simulated product is compared to
 582 real satellite observations.



583 Defining the vertical interpolation error $\boldsymbol{\varepsilon}_{int}$ as:

$$\boldsymbol{\varepsilon}_{int} \equiv \mathbf{W}\mathbf{x}_c^t - \mathbf{x}_f^t \quad (19)$$

584 Eq. (18) can be written as follows:

$$\begin{aligned} \mathbf{y}_m &= H(\mathbf{W}\mathbf{x}_c^t - \mathbf{x}_f^t + \mathbf{W}\boldsymbol{\varepsilon}_m + \mathbf{x}_f^t) \\ &= H(\mathbf{W}\boldsymbol{\varepsilon}_m + \boldsymbol{\varepsilon}_{int} + \mathbf{x}_f^t) \end{aligned} \quad (20)$$

585 Given \mathbf{H} , the Jacobian matrix provided by RTTOV and containing the partial derivatives of $\partial\mathbf{y}/\partial\mathbf{x}$
 586 (i.e. the change in radiance, $\partial\mathbf{y}$, for a change in the state vector, $\partial\mathbf{x}$), Eq.s (17) and (20) can be
 587 approximated, assuming small errors, as follows:

$$\mathbf{y}_{rs} \cong H(\mathbf{x}_f^t) + \mathbf{H}_{\mathbf{x}_f^t} \boldsymbol{\varepsilon}_{rs} \quad (21)$$

$$\mathbf{y}_m \cong H(\mathbf{x}_f^t) + \mathbf{H}_{\mathbf{x}_f^t} (\mathbf{W}\boldsymbol{\varepsilon}_m + \boldsymbol{\varepsilon}_{int}) \quad (22)$$

588 Therefore, the *NWP – GRUAN* comparison in radiance space is expressed as follows:

$$\begin{aligned} \delta\mathbf{y} &\equiv \mathbf{y}_m - \mathbf{y}_{rs} \\ &\cong \mathbf{H}_{\mathbf{x}_f^t} (\mathbf{W}\boldsymbol{\varepsilon}_m + \boldsymbol{\varepsilon}_{int} - \boldsymbol{\varepsilon}_{rs}) \end{aligned} \quad (23)$$

589 Assuming a complete uncorrelation between the interpolation error and those of the radiosonde
 590 and the model, the covariance of the difference is expressed as follows:

$$\mathbf{S}_{\delta\mathbf{y}} \equiv E\{(\partial\mathbf{y} - E\{\partial\mathbf{y}\})^T (\partial\mathbf{y} - E\{\partial\mathbf{y}\})\} \quad (24)$$

591 where E is the expectation operator. We can approximate Eq. (24) as:

$$\mathbf{S}_{\delta\mathbf{y}} \cong \mathbf{H}\mathbf{R}_f^{rs}\mathbf{H}^T + \mathbf{H}\mathbf{W}\mathbf{B}_c^m\mathbf{W}^T\mathbf{H}^T + \mathbf{H}\mathbf{S}_f^{int}\mathbf{H}^T \quad (25)$$

592 where \mathbf{R}_f^{rs} , \mathbf{B}_c^m , and \mathbf{S}_f^{int} are the error covariance matrices of GRUAN measurements (on the fine
 593 grid), the forecast (on the coarse grid), and the vertical interpolation (on the fine grid), respectively,
 594 as described below.

595

596 We first define the GRUAN covariance matrix. GRUAN does not provide a full covariance matrix with
 597 the measurements, therefore \mathbf{R}_f^{rs} is built as a diagonal matrix accounting for the different sources of
 598 uncertainty such as:

$$\begin{aligned} \mathbf{H}\mathbf{R}_f^{rs}\mathbf{H}^T &= \mathbf{H}_T\mathbf{R}_T\mathbf{H}_T^T + \mathbf{H}_q\mathbf{R}_q\mathbf{H}_q^T + \mathbf{H}_p\mathbf{R}_p\mathbf{H}_p^T \\ &\quad + \mathbf{h}_{skinT}u_{skinT}^2\mathbf{h}_{skinT}^T + \mathbf{h}_{T2m}u_{T2m}^2\mathbf{h}_{T2m}^T \\ &\quad + \mathbf{h}_{q2m}u_{q2m}^2\mathbf{h}_{q2m}^T + \mathbf{h}_{p2m}u_{p2m}^2\mathbf{h}_{p2m}^T \end{aligned} \quad (26)$$



599 where \mathbf{R}_T , \mathbf{R}_q , and \mathbf{R}_p are diagonal matrices whose diagonals are the square of GRUAN profiles of
 600 total uncertainty for T , q (converted from RH), and P , respectively, on the Processor vertical grid;
 601 u_{skinT} , u_{T2m} , u_{q2m} , and u_{p2m} the uncertainties associated with the surface parameters (i.e. skin
 602 temperature, 2m temperature, 2m humidity, and 2m pressure) set to 0.3K, 0.3K, 0.04 RH, and
 603 0.1hPa, respectively (Dr. S. Brickmann, DWD, private communication), estimated for the Lindenberg
 604 site. \mathbf{H}_T , \mathbf{H}_q , and \mathbf{H}_p are the Jacobians of the temperature, humidity and pressure profiles,
 605 respectively, and \mathbf{h}_{skinT} , \mathbf{h}_{T2m} , \mathbf{h}_{q2m} , and \mathbf{h}_{p2m} the Jacobians of the surface parameters.

606 \mathbf{R}_T , \mathbf{R}_q , and \mathbf{R}_p are diagonal which precludes a proper propagation of the correlation in radiance
 607 space. In this suboptimal case, \mathbf{R}_f^{rs} , and by extension, $\mathbf{S}_{\delta y}$, the covariance of the comparison, will not
 608 capture the most accurate representation of the uncertainty budget.

609

610 Then, we define the forecast error covariance matrix. For the purposes of this study, the forecast
 611 covariance matrix from the operational Met Office Observation Processing System, a one-
 612 dimensional variational analysis (1D-Var) performed ahead of the main variational process, is used
 613 for \mathbf{B}_f^m . Alternatively, the forecast error covariance matrix can be estimated from an ensemble of
 614 NWP profiles as described in Appendix A.

615

616 Finally, we define vertical interpolation covariance matrix. To estimate \mathbf{S}_f^{int} , the interpolation error
 617 must be quantified.

618 From Eq. (19) we have:

$$\begin{aligned}\boldsymbol{\varepsilon}_{int} &= \mathbf{W}\mathbf{W}^* \mathbf{x}_f^t - \mathbf{x}_f^t \\ &= (\mathbf{W}\mathbf{W}^* - \mathbf{I})\mathbf{x}_f^t\end{aligned}\tag{27}$$

619 where the random vector \mathbf{x}_f^t , representing the true state on the fine grid, is assumed to have
 620 mean $E\{\mathbf{x}_f^t\}$, the (unknown) mean model forecast profile on the fine grid, and covariance
 621 $E\{(\mathbf{x}_f^t - E\{\mathbf{x}_f^t\})^T(\mathbf{x}_f^t - E\{\mathbf{x}_f^t\})\} \equiv \mathbf{B}_f^m$, the covariance of \mathbf{x}_f^t in model space on the fine grid. It
 622 follows that we can express the covariance of the interpolation uncertainty as:

$$\begin{aligned}\mathbf{S}_f^{int} &\equiv E\{(\boldsymbol{\varepsilon}_{int} - E\{\boldsymbol{\varepsilon}_{int}\})^T(\boldsymbol{\varepsilon}_{int} - E\{\boldsymbol{\varepsilon}_{int}\})\} \\ &= (\mathbf{W}\mathbf{W}^* - \mathbf{I})\mathbf{B}_f^m(\mathbf{W}\mathbf{W}^* - \mathbf{I})^T\end{aligned}\tag{28}$$

623 Note that when the model grid coincides with the fine grid we have $\mathbf{W}^* = \mathbf{W}^{-1}$ and $\mathbf{S}_{int} = \mathbf{0}$ as
 624 expected. Replacing \mathbf{W}^* by its form expressed in Appendix B we obtain:

$$\mathbf{S}_f^{int} = \mathbf{B}_f^m(\mathbf{I} - \mathbf{W}(\mathbf{W}^T \mathbf{B}_f^{m-1} \mathbf{W})^{-1} \mathbf{W}^T \mathbf{B}_f^{m-1})\tag{29}$$

625 Note that in practice (i.e. for numerical calculations) it is more convenient to use the form expressed
 626 in Eq. (28) to get \mathbf{S}_f^{int} as a symmetric and positive definite matrix.



627

628 This methodology has been applied to the 587 profiles of the night-time dataset described in the
629 previous section. The covariances $\mathcal{S}_{\delta y}$ of each comparison as approximated in Eq. (25) have been
630 averaged (arithmetic mean, hereafter $\overline{\mathcal{S}_{\delta y}}$) and the square root of the diagonal (i.e. the 1σ standard
631 deviation of the comparison total uncertainty distribution) is shown in figure 6. In practice, we
632 calculate $\mathcal{S}_{\delta y}$ as the sum of the covariance matrices of each variable: the surface measurements
633 covariance (\mathcal{S}_{surf_rs}); the model surface covariance (\mathcal{S}_{surf_m}); the total humidity covariance
634 (\mathcal{S}_{q_total}); the total temperature covariance (\mathcal{S}_{T_total}); and the GRUAN pressure covariance (\mathcal{S}_{p_rs}).
635 The square root of their diagonal is also shown in figure 6. In addition, \mathcal{S}_{q_total} and \mathcal{S}_{T_total} can be
636 further decomposed into the sum of the covariance matrices of each of their components: the
637 GRUAN humidity and temperature covariance (\mathcal{S}_{q_rs} and \mathcal{S}_{T_rs}); the model humidity and
638 temperature covariance (\mathcal{S}_{q_m} and \mathcal{S}_{T_m}); and the covariance of the vertical interpolation of the
639 model humidity and temperature profiles ($\mathcal{S}_{q_m_int}$ and $\mathcal{S}_{T_m_int}$). The square root of their diagonal
640 is also shown in figures 7 and 8.

641 Note that on some occasions, the Processor fine grid does not capture the lowermost or upper most
642 model levels, which caused missing values in \mathbf{W} . The calculation has consequently been done, for
643 those cases, on the remaining levels of \mathbf{W} . It is planned to refine the Processor grid in the future
644 version in order to avoid such missing data in the interpolation matrix.

645

646 As expected, the surface components of the total uncertainty are dominant at frequencies where
647 the radiance is sensitive to the surface (ATMS channels 1-7 and 16-17). Amongst them, the surface
648 component from the model is the largest due to the low confidence in surface emission and
649 properties. Channels with frequencies sensitive to temperature and humidity are dominated by the
650 temperature and humidity total components, respectively.

651 The decomposition of the temperature and humidity total uncertainties in the temperature channels
652 (fig. 7) and in the humidity channels (fig. 8), respectively, shows that, again, the model components
653 are largely dominant. Note that for the highest peaking temperature channel (channel 12) the
654 second largest uncertainty is the GRUAN pressure component. Also, the lowest peaking humidity
655 channels (channels 18-19) are significantly affected by the surface uncertainty, although this may
656 vary with the location and the water vapour burden making those channels peak more or less high in
657 the atmosphere and therefore more or less sensitive to surface.

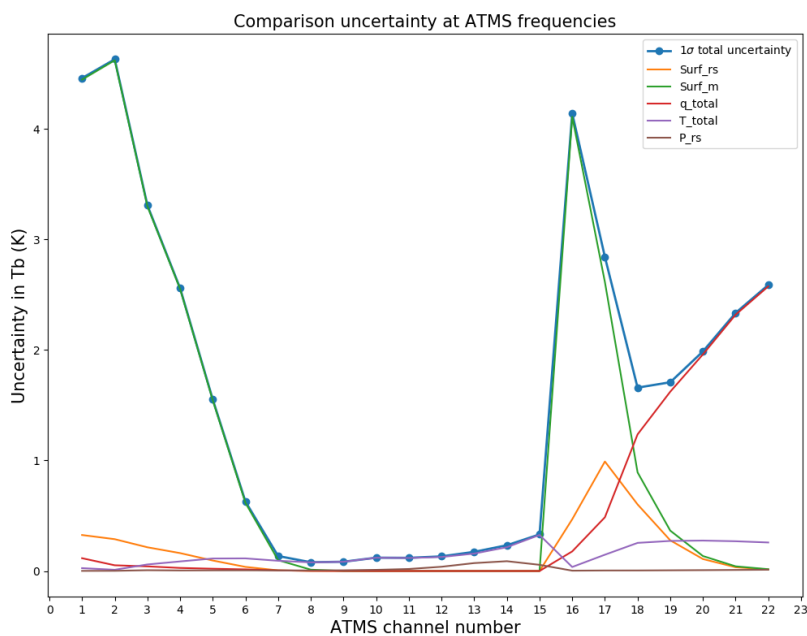
658 The total uncertainty ranges from 0.08 to 0.13K for the temperature channels in figure 7, and from
659 1.6 to 2.5K for the humidity channels in figure 8. Compared to the mean difference $\Delta T_{B_{MetOffice}}$
660 documented in Table 1, the night-time sampling satisfies the consistency requirement of Eq. (1) with
661 $k=1$, noting that the σ term in Eq. (1) that should represent the uncertainty associated with the tri-
662 linear horizontal interpolation, is currently unknown, although assumed small, and therefore
663 ignored. Future work will be dedicated to the estimation of this σ term using high resolution regional
664 model.



665 These preliminary results are in line with the uncertainty range provided by Loew et al. (2017). This
 666 should however be confirmed with the careful evaluation of multiple GRUAN sites over longer time
 667 periods, beyond the scope of this paper but planned to be addressed in the near future.

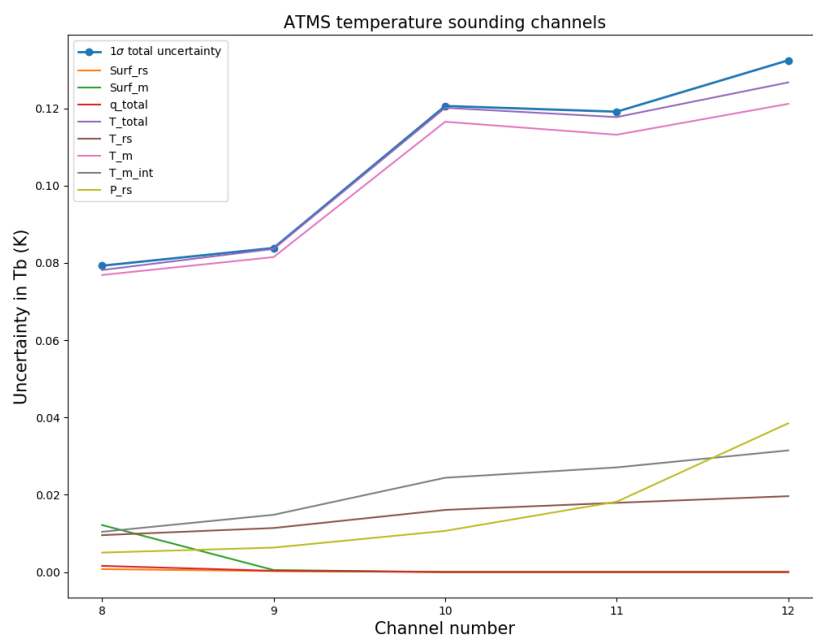
668

669



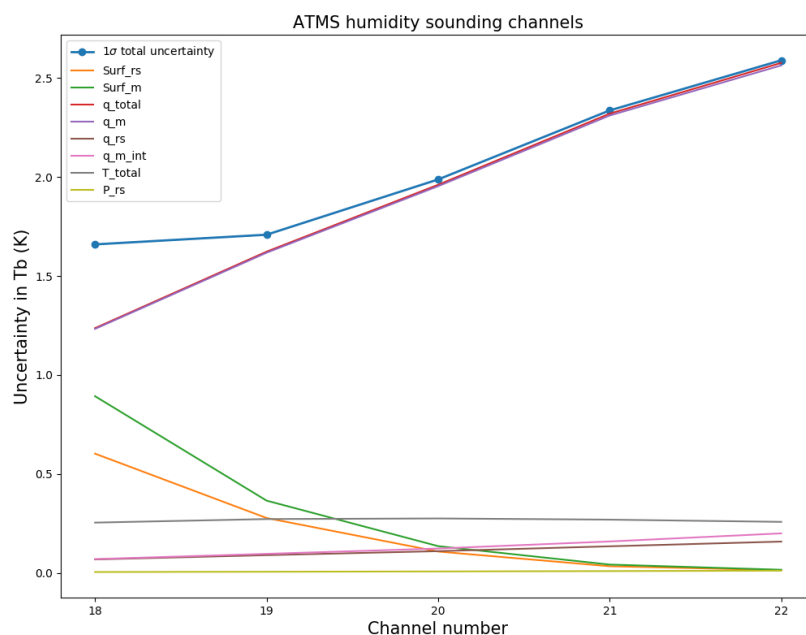
670

671 Figure 6: 1σ standard deviation of the total uncertainty distribution expressed as the square root of
 672 the diagonal of the mean comparison covariance $\overline{\mathcal{S}_{\delta y}}$ (blue dots), and the square root of the
 673 diagonal of the components forming $\overline{\mathcal{S}_{\delta y}}$, namely, the GRUAN surface uncertainty (Surf_rs, orange),
 674 the model surface uncertainty (Surf_m, green), the humidity total uncertainty (q_total, red), the
 675 temperature total uncertainty (T_total, purple), and the GRUAN pressure uncertainty (P_rs, brown).



676

677 Figure 7: Same as figure 6 but only for ATMS temperature upper tropospheric-lower stratospheric
678 channels 8-12, with in addition the square root of the diagonal of the components forming $S_{T_{total}}$,
679 namely, the GRUAN temperature uncertainty (T_{rs} , brown), the model temperature uncertainty
680 (T_m , pink), the model vertical interpolation uncertainty (T_{m_int} , gray).



681

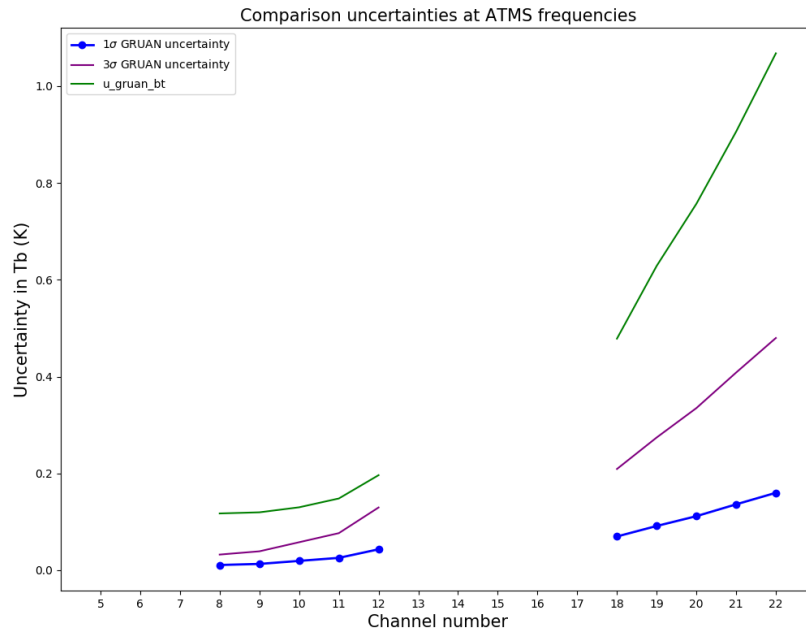
682 Figure 8: Same as figure 6 but only for ATMS humidity tropospheric channels 18-22, with in addition
 683 the square root of the diagonal of the components forming \mathcal{S}_{q_total} , namely, the GRUAN humidity
 684 uncertainty (q_rs , brown), the model humidity uncertainty (q_m , purple), the model vertical
 685 interpolation uncertainty (q_m_int , pink).

686

687 It is interesting to compare the GRUAN processor upper bound uncertainty, calculated assuming a
 688 complete correlation, i.e. u_gruan_bt , with the GRUAN contribution to $\overline{\mathcal{S}_{\delta y}}$. Ignoring the
 689 uncertainties associated with the surface parameters, the GRUAN contribution to $\overline{\mathcal{S}_{\delta y}}$ can be
 690 calculated as the square root of the first three term of Eq. (26). Figure 9 shows that u_gruan_bt is
 691 consistently four times larger than the 3σ standard deviation of the GRUAN contribution to $\overline{\mathcal{S}_{\delta y}}$
 692 at the frequencies of interest. It may indicate that the assumption of complete correlation in the
 693 uncertainty (i.e. the use of GRUAN total uncertainty as if correlated at all levels), associated with the
 694 calculation of the maximal total uncertainty in Tb results in a large overestimation of the uncertainty
 695 in radiance space. In addition, it should be remembered that the use of diagonal matrices in Eq. (26)
 696 is suboptimal and may not capture the full extent of the uncertainty. The lack of explicit systematic
 697 and random errors associated with the radiosonde profiles and the lack of discretisation between
 698 correlated and uncorrelated uncertainty components in GRUAN products is also suboptimal. This
 699 stresses the need for the GRUAN community to provide proper covariance matrices, better defined
 700 error profiles, and better discretisation of correlated and uncorrelated uncertainties. Finally, it is
 701 possible, although not likely, that a violation of the assumption of ‘small’ uncertainties in Eq.s (21-



702 22) could result in non-linear perturbations potentially causing the GRUAN contribution to $\overline{\mathcal{S}_{\delta y}}$ to be
 703 underestimated.
 704



705

706 Figure 9: 1σ standard deviation of the uncertainty distribution from GRUAN contribution to $\overline{\mathcal{S}_{\delta y}}$ is
 707 shown in blue (dotted line). It is calculated as the square root of the first three term of Eq. (26), i.e.
 708 $\sqrt{\text{diag}(\mathcal{S}_{q,rs} + \mathcal{S}_{T,rs} + \mathcal{S}_{P,rs})}$. The 3σ standard deviation of the uncertainty distribution is shown in
 709 purple (solid line). $u_{\text{gruan_bt}}$, the GRUAN uncertainty propagated into radiance space by the
 710 GRUAN Processor and averaged over the night-time sample is shown in green (solid line).

711

712 Next, the overall agreement between the Met Office model and GRUAN, in radiance space, is
 713 assessed via a χ^2 test. Here, a reduced χ^2 , hereafter $\tilde{\chi}^2$, is estimated for each profile as follows:

$$\tilde{\chi}^2 = \frac{1}{c} (\delta \mathbf{y}_i - \overline{\delta \mathbf{y}})^T \mathcal{S}_{\delta \mathbf{y}}^{-1} (\delta \mathbf{y}_i - \overline{\delta \mathbf{y}}) \quad (30)$$

714

715 where $\delta \mathbf{y}_i$ is the $NWP - GRUAN$ difference in Tb for the i^{th} comparison, $\overline{\delta \mathbf{y}}$ the mean comparison
 716 over the sample. The number of degrees of freedom c , in this context, is the number of channels
 717 regardless any constraints as defined in Rodgers, 2000 (section 12.2).

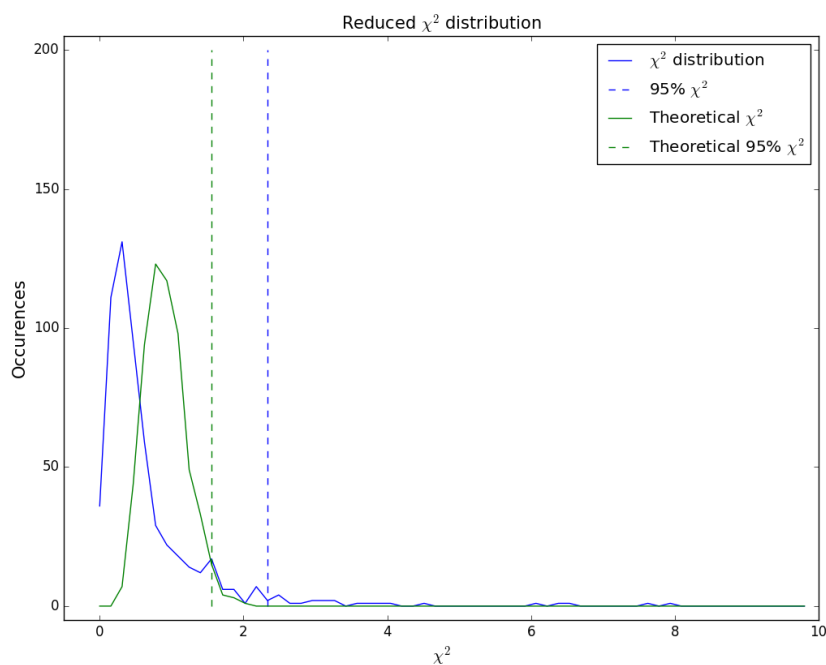


718

719 Comparing calculated and theoretical \bar{X}^2 will allow, in theory, the assessment and eventually
720 revision of the uncertainty estimates used for the NWP model and GRUAN. Figure 10 shows the
721 distribution of \bar{X}^2 calculated for the night-time sampling (blue line) and how it compares to the
722 theoretical \bar{X}^2 estimated from random data of similar sampling size (green line). Dashed lines show
723 the 95-percentile of each distribution. \bar{X}^2 values beyond the theoretical 95-percentile line reflect the
724 comparisons where the model and GRUAN are significantly different. For this example, the 95-
725 percentile of the calculated \bar{X}^2 (blue dashed line) is 5% larger than the theoretical one (green dashed
726 line): i.e. about 10% of the calculated \bar{X}^2 are greater than the theoretical 95-percentile threshold.
727 This relatively good match between calculated and theoretical \bar{X}^2 rules out the hypothesis of the
728 violation of small uncertainties in Eq.s (21-22). However, it might be that one (or more) component
729 of $S_{\delta y}$ have been underestimated and could be revised until both 95-percentiles match. It is also
730 possible that unforeseen sources of uncertainty have been unaccounted for in Eq. (25). In both
731 cases, the increased total uncertainty will reduce the number of comparisons failing the test and
732 reduce the difference between the calculated and theoretical 95-percentile threshold.

733 A refined assessment using a larger sample spanning several years and several GRUAN sites will be
734 addressed as part of future work, but is out of scope of this study.

735



736

737 Figure 10: Reduced \bar{X}^2 distribution from the NWP – GRUAN night-time sampling (blue) and



738 theoretical reduced X^2 estimated from a random sampling of equal size and equal degrees of
739 freedom (blue). Dashed lines show the 95-percentile of each distribution.

740

741 6. Conclusion

742 Numerical weather prediction models have demonstrated ability to act as suitable reference
743 comparators for the calibration and validation of satellite instruments. Model analysis and short-
744 range forecast uncertainties are incrementally reduced by progressive improvements in data
745 assimilation techniques and the ingestion of a large and growing number of observations from
746 multiple sources. From the state-of-the-art of NWP output fields, biases as small as a tenth of a
747 Kelvin can be highlighted in some satellite datasets. In addition, NWP models provide global fields,
748 which allow for the evaluation of satellite data across the full dynamic range of the instrument. Yet
749 model uncertainty estimates do not meet international metrological traceability standards as
750 provided by other reference datasets, such as the GRUAN radiosondes.

751

752 In order to address the missing links in the traceability chain of model uncertainty, a collocation and
753 radiance simulation tool (the GRUAN Processor) has been developed in the framework of the GAIA-
754 CLIM project. This allows us to quantify differences between GRUAN radiosonde profiles of well-
755 defined uncertainties and NWP fields, in both observation and radiance space.

756 Based on the radiative transfer core capability of the radiance simulator developed and maintained
757 by NWP SAF, the Processor collocates model fields to GRUAN radiosonde profiles in space and time,
758 then simulates top-of-atmosphere brightness temperatures for both datasets at frequencies used by
759 satellite instruments, and propagates GRUAN uncertainties in radiance space. The details of the
760 GRUAN Processor have been described in this paper and a mathematical methodology aimed at
761 assessing *NWP – GRUAN* comparisons in radiance space has been expounded.

762

763 For this study, a small sampling of 573 daytime and 587 night-time GRUAN radiosonde profiles from
764 Lindenberg, Germany, in 2016, and matching NWP fields from the Met Office and ECMWF global
765 models have been processed and analysed to demonstrate the GRUAN Processor capability.

766 In the geophysical space of the radiosonde observations, the *NWP – GRUAN* comparison has
767 highlighted 0.5K cold biases located in the stratosphere of the ECMWF model and in the lower
768 troposphere of the Met Office model. A wet bias ranging from 50 to 75% of the local specific
769 humidity is visible in both models at pressure between 200 and 100hPa.

770 In radiance space, the Met Office and ECMWF T_b are found to be within $\pm 0.09K$ and $\pm 0.39K$,
771 respectively, to GRUAN night-time profiles (when GRUAN biases are minimal), at frequencies
772 predominantly sensitive to temperature (54-57GHz) in the vertical domain where GRUAN
773 radiosonde observations are available. Similarly, the Met Office and ECMWF T_b are found to be
774 within $\pm 0.46K$ and $\pm 0.37K$, respectively, to GRUAN night-time profiles at frequencies predominantly
775 sensitive to humidity (around 183GHz).



776

777 The propagation of GRUAN uncertainties in radiance space is performed in the GRUAN Processor via
778 perturbation of the temperature, humidity and pressure profiles by plus and minus their total
779 uncertainty as provided in the RS92-GDP data files. This process assumes a complete correlation of
780 the uncertainties at all levels. This is a pessimistic assumption and the resulting uncertainty obtained
781 in radiance space is therefore representative of a maximum uncertainty of the GRUAN component
782 (the model uncertainty is not accounted for). The true GRUAN uncertainty in radiance space is
783 smaller than that calculated as only a fraction of GRUAN total uncertainty (in observation space) is
784 really correlated over the entire profile.

785 Independently from that maximum GRUAN uncertainty estimate, a rigorous estimation of the
786 uncertainties in radiance space associated with the *NWP – GRUAN* difference is proposed in this
787 study as a post-processing application based on the GRUAN Processor outputs. The covariance of
788 this difference, $S_{\delta y}$, is calculated as the sum of the GRUAN, model, and interpolation uncertainties
789 propagated in radiance space.

790 Tested with the Met Office background error covariance, the NWP component of $S_{\delta y}$ is found to be
791 the dominant source of uncertainty. The total uncertainty of the difference ranges from 0.08 to
792 0.13K at frequencies sensitive to temperature and from 1.6 to 2.5K at frequencies sensitive to
793 humidity, satisfying, on average, the consistency check (Eq. 1) for night-time profiles.

794 The GRUAN component of $S_{\delta y}$ is found to be four times smaller (at 3σ) than the maximum GRUAN
795 uncertainty estimated in the Processor, demonstrating the large overestimation of the complete
796 correlation assumption. However, it is worth stressing that in absence of covariance information,
797 error (random and systematic) characterisation, and discretisation between correlated and
798 uncorrelated uncertainty components in GRUAN data files, the estimation of $S_{\delta y}$ remains
799 suboptimal.

800 The X^2 distribution calculated for the comparisons between model-based (Met Office) and GRUAN-
801 based simulated T_b revealed that the number of significantly different comparisons is close although
802 slightly larger than that of the corresponding theoretical X^2 distribution. Implications are that either
803 one or several components of $S_{\delta y}$ are underestimated, or that a source of uncertainty has been
804 overlooked.

805

806 The next step will be to process and analyse collocated profiles spanning several years and multiple
807 GRUAN sites. This will provide a better, although incomplete, geographical distribution of model
808 biases as well as their evolution in time. Away from the surface, NWP model biases are to first order
809 a function of latitude and height, and can usefully be studied for polar, mid-latitude and tropical
810 bands. For northern latitude bands, the NWP uncertainties can be studied by comparison with
811 GRUAN observations, but for the tropics and southern latitudes, where there are few or no GRUAN
812 data, these could to be supplemented with other high quality radiosonde reports. The aim will be to
813 provide a refined set of model uncertainty for selected frequencies spanning both microwave and
814 infrared domains. Ultimately, the contribution from this work will help draw the full model
815 uncertainty budget (composed of uncertainties in radiance space, radiative transfer modelling, scale



816 mismatch, and cloud residual) for more robust assessment of satellite observations. Finally, the
817 larger sampling will also ensure a more robust X^2 analysis and, if deemed necessary, help revise the
818 model covariance matrices used in operation at the Met Office and ECMWF.

819 The quantitative estimate of errors and uncertainties in NWP models, both temperature, humidity,
820 and radiance space, could aid in the interpretation of observation minus short-range forecast
821 statistics for satellite instruments, for example by helping to identify whether biases in observation-
822 minus-model background values could be due to systematic errors in the NWP model short-range
823 forecasts. In future work, it is planned to use the GRUAN processor output to evaluate biases in
824 observation-minus-model background statistics of satellite data.

825 Finally, the GRUAN processor will also evolve with the evolution of RTTOV. For example, a parallel
826 version of the Processor is currently being tested with the fast radiative transfer model RTTOV
827 Ground-based (RTTOV-gb). RTTOV-gb is a modified version of RTTOV that allow for simulations of
828 ground-based upward-looking microwave sensors (De Angelis et al., 2016). Model and GRUAN
829 simulated Tb and propagated uncertainties are expected to help estimate the uncertainties in the
830 microwave radiometer observations for which RTTOV-gb has been developed. It is also planned to
831 upgrade the Processor in order to support RTTOV 12 (Hocking et al., 2017). This upgrade will allow
832 the better handling of surface emissivity and give the option to output principal components (PC)
833 used for the new generation of hyperspectral infrared sounders. Note that other fast radiative
834 transfer models, such as the Community Radiative Transfer Model (CRTM), could potentially be
835 tested with the GRUAN Processor, although there is no immediate plan to do so.

836

837 Appendix A: Forecast error covariance matrix estimation

838 If the forecast error covariance matrix from the NWP forecast model used as input to the Processor
839 is not available, it can be determined from an ensemble of K NWP profiles, with $K > N$ where N is the
840 number of vertical levels, such that:

$$B_c^m = \frac{X'X'^T}{K-1} \quad (A1)$$

841 where $K-1$ gives the best estimate of the covariance of the population from which the sample K is
842 drawn, and with X' such as:

$$X' = (x_c^{m1} - \overline{x_c^m}, \dots, x_c^{mj} - \overline{x_c^m}, \dots, x_c^{mK} - \overline{x_c^m}) \quad (A2)$$

843 where x_c^{mj} is the j^{th} model profile of the K ensemble, and $\overline{x_c^m}$ is the mean of the K profiles, both on
844 the coarse model vertical grid.

845

846 Appendix B: Interpolation matrix pseudo inverse

847 The interpolation matrix W is not square and therefore its inverse cannot be calculated. Instead, a
848 pseudo inverse, W^* , can be to express using, for example, the weighted least square estimate of x_c^t
849 (Rodgers, 2000). For that, we need to minimize:



$$\mathbf{r} = \frac{1}{2}(\mathbf{x}_f^t - \mathbf{W}\mathbf{x}_c^t)^T \mathbf{B}_f^{m-1}(\mathbf{x}_f^t - \mathbf{W}\mathbf{x}_c^t) \quad (\text{B1})$$

850 where, for the weight, we use the forecast error covariance matrix expressed on the fine grid, \mathbf{B}_f^m ,
 851 since we interpolate the model profiles on that grid.

852 By taking the derivative with respect to \mathbf{x}_c^t and setting it to zero, we find:

$$\mathbf{x}_c^t = (\mathbf{W}^T \mathbf{B}_f^{m-1} \mathbf{W})^{-1} \mathbf{W}^T \mathbf{B}_f^{m-1} \mathbf{x}_f^t \quad (\text{B2})$$

853 where.

$$\mathbf{W}^* = (\mathbf{W}^T \mathbf{B}_f^{m-1} \mathbf{W})^{-1} \mathbf{W}^T \mathbf{B}_f^{m-1} \quad (\text{B3})$$

854 In order to find an expression for \mathbf{B}_f^m , we refer to \mathbf{B}_c^m , the forecast covariance matrix on the coarse
 855 model grid, to calculate the forecast error correlation matrix \mathbf{C}_c^m , on the coarse model grid. The
 856 correlation matrix is then reconditioned on the fine Processor grid, and referred to as \mathbf{C}_f^{rec} , as
 857 explained below.

858 Defining $\mathbf{\Sigma}$, a diagonal matrix representing the square root of \mathbf{B}_c^m variance, such as:

$$\mathbf{\Sigma} = \sqrt{\text{diag}(\mathbf{B}_c^m)} \quad (\text{B4})$$

859 \mathbf{C}_m can be expressed as:

$$\mathbf{C}_m = \mathbf{\Sigma}^{-1} \mathbf{B}_c^m \mathbf{\Sigma}^{-1} \quad (\text{B5})$$

860 We can then define \mathbf{C}_f^m as:

$$\mathbf{C}_f^m = \mathbf{W} \mathbf{C}_c^m \mathbf{W}^T \quad (\text{B6})$$

861 However, Eq. (B6) does not guarantee that \mathbf{C}_f^m diagonal elements are equal to one. This constraint
 862 needs to be imposed such as:

$$\mathbf{C}_f^{rec} = \mathbf{W} \mathbf{C}_c^m \mathbf{W}^T - \text{diag}(\mathbf{W} \mathbf{C}_c^m \mathbf{W}^T) + \mathbf{I} \quad (\text{B7})$$

863 Given σ_m , a vector composed of the square root of the variance of $\boldsymbol{\varepsilon}_m$ variance, \mathbf{B}_f^m is expressed as
 864 follows:

$$\mathbf{B}_f^m = \text{diag}(\mathbf{W} \sigma_m) \mathbf{C}_f^{rec} \text{diag}(\mathbf{W} \sigma_m) \quad (\text{B8})$$

865

866 Data availability

867 For further information on the GRUAN Processor source code and/or outputs availability, please
 868 contact the lead author (fabien.carminati@metoffice.gov.uk).

869



870 Competing interests

871 The authors declare that they have no conflict of interest.

872

873 Acknowledgment

874 This work and its contributors (Fabien Carminati, Stefano Migliorini, Bruce Ingleby, Bill Bell, Heather
875 Lawrence, and Stu Newman) were supported by the European Union's Horizon 2020 research and
876 innovation programme under the GAIA-CLIM grant agreement No. 640276.

877

878 References

879 Auligné, T. , McNally, A. P. and Dee, D. P.: Adaptive bias correction for satellite data in a numerical
880 weather prediction system, *Q.J.R. Meteorol. Soc.*, 133: 631-642, doi:10.1002/qj.56, 2007.

881 Bauer, P., Thorpe, A., and Brunet, G.: The quiet revolution of numerical weather prediction, *Nature*,
882 525, 47, doi:10.1038/nature14956 , 2015.

883 Bell, W., Candy, B., Atkinson, N., Hilton, F., Baker, N., Bormann, N., Kelly, G., Kazumori, M., Campbell,
884 W. F., and Swadley, S. D.: The assimilation of SSMIS radiances in numerical weather prediction
885 models, *IEEE Transactions on Geoscience and Remote Sensing*, 46, 884–900, doi:
886 10.1109/TGRS.2008.917335, 2008.

887 Bojinski, S., Verstraete, M., Peterson, T. C., Richter, C., Simmons, A., and Zemp, M.: The concept of
888 essential climate variables in support of climate research, applications, and policy, *Bulletin of the*
889 *American Meteorological Society*, 95, 1431–1443, <https://doi.org/10.1175/BAMS-D-13-00047.1>,
890 2014.

891 Bonavita, M., Hólm, E.V., Isaksen, L., Fisher, M.: The evolution of the ECMWF hybrid data
892 assimilation system, *Q. J. R. Meteorol.Soc.*, 142, 287-303, doi:10.1002/qj.2652, 2016.

893 Bormann, N., Fouilloux, A., and Bell, W.: Evaluation and assimilation of ATMS data in the ECMWF
894 system, *Journal of Geophysical Research: Atmospheres*, 118, 12.970–12.980,
895 doi:10.1002/2013JD020325, 2013.

896 Calbet, X., Peinado-Galan, N., Rípodas, P., Trent, T., Dirksen, R., and Sommer, M.: Consistency
897 between GRUAN sondes, LBLRTM and IASI, *Atmos. Meas. Tech.*, 10, 2323-2335,
898 <https://doi.org/10.5194/amt-10-2323-2017>, 2017.

899 Courtier, P. , Thépaut, J. and Hollingsworth, A.: A strategy for operational implementation of 4D-Var,
900 using an incremental approach. *Q.J.R. Meteorol. Soc.*, 120: 1367-1387,
901 doi:10.1002/qj.49712051912, 1994.

902 De Angelis, F., Cimini, D., Hocking, J., Martinet, P., and Kneifel, S.: RTTOV-gb – adapting the fast
903 radiative transfer model RTTOV for the assimilation of ground-based microwave radiometer



- 904 observations, *Geosci. Model Dev.*, 9, 2721–2739, <https://doi.org/10.5194/gmd-9-2721-2016>,
905 2016.
- 906 Dee, D.: Variational bias correction of radiance data in the ECMWF system, in Proc. of the ECMWF
907 Workshop on Assimilation of High Spectral Resolution Sounders in NWP, Vol. 28, pp. 97–112,
908 <https://www.ecmwf.int/search/elibrary>, 2004.
- 909 Dirksen, R. J., Sommer, M., Immler, F. J., Hurst, D. F., Kivi, R., and Vömel, H.: Reference quality upper-
910 air measurements: GRUAN data processing for the Vaisala RS92 radiosonde, *Atmos. Meas. Tech.*,
911 7, 4463–4490, <https://doi.org/10.5194/amt-7-4463-2014>, 2014.
- 912 Eyre, J.: A fast radiative transfer model for satellite sounding systems, ECMWF Tech. Memo 176,
913 <https://www.ecmwf.int/search/elibrary>, 1991.
- 914 Green, P., Gardiner, T., Medland, D., Cimini, D.: Guide to Uncertainty in Measurement & its
915 Nomenclature, GAIA-CLIM Deliverable D2.6 <http://www.gaia-clim.eu/>, 2018.
- 916 Han, W. and Bormann, N.: Constrained adaptive bias correction for satellite radiance assimilation in
917 the ECMWF 4D-Var system. ECMWF Technical Memorandum 783,
918 <https://www.ecmwf.int/search/elibrary>, 2016.
- 919 Haseler, J.: Early-delivery suite. ECMWF Technical Memorandum No. 454,
920 <https://www.ecmwf.int/search/elibrary>, 2004.
- 921 Hocking, J., Rayer, P., Rundle, D., Saunders, R., Matricardi, M., Geer, A., Brunel, P., and Vidot, J.:
922 RTTOV v12 Users Guide, Tech. Rep. NWPSAF-MO-UD-037, EUMETSAT Satellite Application Facility
923 on Numerical Weather Prediction (NWPSAF),
924 <https://www.nwpsaf.eu/site/software/rttov/documentation/>, 2017.
- 925 Hocking, J., Rayer, P., Rundle, D., Saunders, R., Matricardi, M., Geer, A., Brunel, P., and Vidot, J.:
926 RTTOV v11 Users Guide, Tech. Rep. NWPSAF-MO-UD-028, EUMETSAT Satellite Application Facility
927 on Numerical Weather Prediction (NWPSAF), [https://www.nwpsaf.eu/site/software/rttov/rttov-
928 v11/](https://www.nwpsaf.eu/site/software/rttov/rttov-v11/), 2015.
- 929 Hollmann, R., Merchant, C. J., Saunders, R., Downy, C., Buchwitz, M., Cazenave, A., Chuvieco, E.,
930 Defourny, P., de Leeuw, G., Forsberg, R., Holzer-Popp, T., Paul, F., Sandven, S., Sathyendranath,
931 S., van Roozendaal, M. and Wagner, W.: The ESA climate change initiative: Satellite data records
932 for essential climate variables, *Bulletin of the American Meteorological Society*, 94, 1541–1552,
933 <https://doi.org/10.1175/BAMS-D-11-00254.1>, 2013.
- 934 Hyland, R. W., Wexler, A. Formulation for the thermodynamic properties of the saturated phases of
935 H₂O from 173.15K to 473.15K. *ASHRAE Trans.*, 89(2A), 500–519, 1983.
- 936 Immler, F. J., Dykema, J., Gardiner, T., Whiteman, D. N., Thorne, P. W., and Vömel, H.: Reference
937 Quality Upper-Air Measurements: guidance for developing GRUAN data products, *Atmos. Meas.*
938 *Tech.*, 3, 1217–1231, <https://doi.org/10.5194/amt-3-1217-2010>, 2010.
- 939 Ingleby, B.: An assessment of different radiosonde types 2015/2016, European Centre for Medium
940 Range Weather Forecasts, <https://www.ecmwf.int/search/elibrary>, 2017.



- 941 Ingleby, B. and Edwards, D.: Changes to radiosonde reports and their processing for numerical
942 weather prediction, *Atmospheric Science Letters*, 16: 44-49, doi:10.1002/asl2.518, 2015.
- 943 Ingleby, N., Lorenc, A., Ngan, K., Rawlins, F., and Jackson, D.: Improved variational analyses using a
944 nonlinear humidity control variable, *Quarterly Journal of the Royal Meteorological Society*, 139:
945 1875-1887, doi:10.1002/qj.2073, 2013.
- 946 Joo, S., Eyre, J., and Marriott, R.: The impact of Metop and other satellite data within the Met Office
947 global NWP system using an adjoint-based sensitivity method, *Monthly Weather Review*, 141,
948 3331–3342, <https://doi.org/10.1175/MWR-D-12-00232.1>, 2013.
- 949 Kazumori, M. and English, S. J.: Use of the ocean surface wind direction signal in microwave radiance
950 assimilation, *Quarterly Journal of the Royal Meteorological Society*, 141: 1354-1375,
951 doi:10.1002/qj.2445, 2015.
- 952 Lesht, B., Miloshevich, L., and Liljegren, J.: Comparison of ECMWF model analyses with the observed
953 upperair temperature and relative humidity climatology at the ARM NSA, SGP, and TWP Climate
954 Research Facility Sites, in Proc. 14th Atmospheric Radiation Measurement (ARM) Science Team
955 Meeting, Albuquerque, New Mexico, March 22-26, 2004.
- 956 Leutbecher, M., Lock, S., Ollinaho, P., Lang, S. T., Balsamo, G., Bechtold, P., Bonavita, M.,
957 Christensen, H. M., Diamantakis, M., Dutra, E., English, S., Fisher, M., Forbes, R. M., Goddard, J.
958 , Haiden, T., Hogan, R. J., Juricke, S., Lawrence, H., MacLeod, D., Magnusson, L., Malardel, S.,
959 Massart, S., Sandu, I., Smolarkiewicz, P. K., Subramanian, A., Vitart, F., Wedi, N. and
960 Weisheimer, A.: Stochastic representations of model uncertainties at ECMWF: state of the art
961 and future vision. *Q.J.R. Meteorol. Soc*, 143: 2315-2339. doi:10.1002/qj.3094, 2017.
- 962 Loew, A., Bell, W., Brocca, L., Bulgin, C.E., Burdanowitz, J., Calbet, X., Donner, R.V., Ghent, D., Gruber,
963 A., Kaminski, T. and Kinzel, J., Klepp, C., Lambert, J. C., Schaepman-Strub, G., Schröder, M.,
964 Verhoelst, T.: Validation practices for satellite based earth observation data across communities,
965 *Reviews of Geophysics*, 55, 779–817, doi:10.1002/2017RG000562, 2017.
- 966 Lorenc, A. C., Ballard, S. P., Bell, R. S., Ingleby, N. B., Andrews, P. L., Barker, D. M., Bray, J. R., Clayton,
967 A. M., Dalby, T., Li, D., Payne, T. J. and Saunders, F. W.: The Met. Office global three-dimensional
968 variational data assimilation scheme, *Quarterly Journal of the Royal Meteorological Society*, 126:
969 2991-3012, doi:10.1002/qj.49712657002, 2000.
- 970 Lu, Q. and Bell, W.: Characterizing channel center frequencies in AMSU-A and MSU microwave
971 sounding instruments, *Journal of Atmospheric and Oceanic Technology*, 31, 1713–1732,
972 <https://doi.org/10.1175/JTECH-D-13-00136.1>, 2014.
- 973 Lupu, C., Geer, A. J.: Operational Implementation of RTTOV-11 in the IFS. ECMWF Tech. Memo. 748,
974 <https://www.ecmwf.int/search/elibrary>, 2015
- 975 Massonnet, F., Bellprat, O., Guemas, V., and Doblas-Reyes, F. J.: Using climate models to estimate
976 the quality of global observational data sets, *Science*, doi:10.1126/science.aaf6369, 2016.



- 977 Paufler, P.: Landolt-Börnstein: Numerical data and functional relationships in science and
978 technology, Ed. by O. Madelung Springer-Verlag Berlin, 23: 1360-1360,
979 doi:10.1002/crat.2170231029, 1988.
- 980 Rawlins, F., Ballard, S., Bovis, K., Clayton, A., Li, D., Inverarity, G., Lorenc, A., and Payne, T.: The Met
981 Office global four-dimensional variational data assimilation scheme, Quarterly Journal of the
982 Royal Meteorological Society, 133: 347-362, doi:10.1002/qj.32, 2007.
- 983 Rodgers CD. Inverse methods for atmospheric sounding: theory and practice. World scientific; 2000.
- 984 Saunders, R., Matricardi, M., and Brunel, P.: An improved fast radiative transfer model for
985 assimilation of satellite radiance observations, Quarterly Journal of the Royal Meteorological
986 Society, 125: 1407-1425, doi:10.1002/qj.1999.49712555615, 1999.
- 987 Saunders, R., Rayer, P., Blackmore, T., Matricardi, M., Bauer, P., and Salmond, D.: A new fast
988 radiative transfer model-RTTOV-9, in Proc. Joint 2007 EUMETSAT Meteorological Satellite
989 Conference and the 15th Satellite Meteorology and Oceanography Conference of the American
990 Meteorological Society, Amsterdam, The Netherlands, 2007.
- 991 Saunders, R., Hocking, J., Turner, E., Rayer, P., Rundle, D., Brunel, P., Vidot, J., Rocquet, P.,
992 Matricardi, M., Geer, A., Bormann, N., and Lupu, C.: An update on the RTTOV fast radiative
993 transfer model (currently at version 12), Geosci. Model Dev. Discuss.,
994 <https://doi.org/10.5194/gmd-2018-64>, in review, 2018.
995
- 996 Simmons, A., Untch, A., Jakob, C., Kållberg, P., and Unden, P.: Stratospheric water vapour and
997 tropical tropopause temperatures in ECMWF analyses and multi-year simulations, Quarterly
998 Journal of the Royal Meteorological Society, 125: 353-386, doi:10.1002/qj.49712555318, 1999.
- 999 Smith, A.: Radiance simulator v2.0 user guide, EUMETSAT Satellite Application Facility on Numerical
1000 Weather Prediction (NWPSAF), Tech. Rep. NWPSAF-MO-UD-040,
1001 <https://www.nwpsaf.eu/site/software/radiance-simulator/documentation/>, 2014.
- 1002 Sommer, M., Dirksen, R., and Rohden, C.: Brief Description of the RS92 GRUAN Data Product (RS92-
1003 GDP), Technical Document GRUAN-TD-4, <https://www.gruan.org/documentation/gruan/td/>,
1004 2011.
- 1005 Thorne, P. W., Madonna, F., Schulz, J., Oakley, T., Ingleby, B., Rosoldi, M., Tramutola, E., Arola, A.,
1006 Buschmann, M., Mikalsen, A. C., Davy, R., Voces, C., Kreher, K., De Maziere, M., and Pappalardo,
1007 G.: Making better sense of the mosaic of environmental measurement networks: a system-of-
1008 systems approach and quantitative assessment, Geosci. Instrum. Method. Data Syst., 6, 453-472,
1009 <https://doi.org/10.5194/gi-6-453-2017>, 2017.
- 1010 Zeng, Y., Su, Z., Calvet, J. C., Manninen, T., Swinnen, E., Schulz, J., Roebeling, R., Poli, P., Tan, D.,
1011 Riihelä, A., Tanis, C. M., Arslan, A. N., Obregon, A., Kaiser-Weiss, A., John, V. O., Timmermans, W.,
1012 Timmermans, J., Kaspar, F., Gregow, H., Barbu, A. L., Fairbairn, D., Gelati, E., Meurey, C.: Analysis
1013 of current validation practices in Europe for space-based climate data records of essential climate
1014 variables, International Journal of Applied Earth Observation and Geoinformation, Volume 42,
1015 Pages 150-161, ISSN 0303-2434, <https://doi.org/10.1016/j.jag.2015.06.006>, 2015.



1016 Zou, X., Wang, X., Weng, F., and Li, G.: Assessments of Chinese FengYun Microwave Temperature
1017 Sounder (MWTS) measurements for weather and climate applications, *Journal of Atmospheric
1018 and Oceanic Technology*, 28, 1206–1227, <https://doi.org/10.1175/JTECH-D-11-00023.1>, 2011.
1019